

Highlights

Hydrogen-blended fuels: nonlinear flame dynamics and safe operation limits

Sreenath Malamal Gopinathan, Aswathy Surendran, Maria A. Heckl

- Laminar flame dynamics is always nonlinear, even at very low amplitudes.
- Flames are effectively shortened by high-amplitude excitation.
- Stability analysis for micromix combustion rig is made with Green's function approach.
- Increase in hydrogen concentration reduces risk of instability.

Citation: Gopinathan, S. M., Surendran, A. and Heckl, M. A. (2025), "Hydrogen-blended fuels: Non-linear flame dynamics and safe operation limits", *International Journal of Hydrogen Energy*, 111: pp. 371–384. doi:[10.1016/j.ijhydene.2025.02.172](https://doi.org/10.1016/j.ijhydene.2025.02.172)

Preprint

Hydrogen-blended fuels: nonlinear flame dynamics and safe operation limits

Sreenath Malamal Gopinathan^{a,*}, Aswathy Surendran^b and Maria A. Heckl^{a,c}

^aSchool of Chemical and Physical Sciences, Keele University, Staffordshire ST5 5BG, United Kingdom

^bDepartment of Aerospace Engineering, Indian Institute of Technology Madras, Chennai 600036, India

^cThermo-Fluid Dynamics Group, School of Engineering and Design, Technical University of Munich, Boltzmannstr. 15, Garching 85748, Germany

ARTICLE INFO

Keywords:

nonlinear flame dynamics
hydrogen-blend flames
perturbation travel times
Green's function
stability analysis
flashback

ABSTRACT

This paper presents a two-part study on laminar hydrogen-blend flames in a micromix combustion test rig. The first part of the study focuses on the nonlinear dynamics of the flame, which is modelled by the G-equation. The laminar flame speed and the amplitude of convected velocity perturbations are the key parameters. Both have a marked effect on the travel times associated with the convected perturbations. These travel times are quantified and represented as functions of the laminar flame speed and the perturbation amplitude. The second part of the study considers a combustion test rig with the hydrogen-blend flame considered in the first part. A Green's function approach is used to calculate the complex eigenfrequencies of the complete combustion system. The key parameters are the hydrogen concentration, equivalence ratio and amplitude of velocity fluctuations. The following regions are identified in this 3-D parameter space: regions of thermoacoustic instability, stable limit cycles and flame flashback. This information gives the safe operation limits.

1. Introduction

Hydrogen is a promising facilitator of energy generation with net-zero carbon emissions. Therefore, the combustion of hydrogen and hydrogen-enriched hydrocarbon gases has become a hot research topic in recent years. There is potential for clean combustion in several sectors, in particular

- domestic and industrial heating systems [1–3]
- gas turbine engines [4, 5]
- industrial furnaces [6]

If a conventional hydrocarbon fuel is enriched with a small amount of hydrogen (up to 30% by volume), the corresponding flame behaves much like a flame without the enrichment. This was exploited in the HyDeploy trial at Keele University [<https://hydeploy.co.uk/>], which inspired the current paper. Starting in 2019, hydrogen was added to the private gas network of Keele University's campus; 100 homes and 30 university buildings received the blended gas. The results showed that up to 20% hydrogen could be added to the gas network without any negative impact on the existing equipment, such as boilers and cookers. Glanville et al. [7] tested different combustion appliances by operating them with a methane-hydrogen fuel blend containing 0–30% hydrogen (by volume). All appliances worked well, as the flame behaved much like a pure methane flame within this range of hydrogen enrichment.


However, if hydrocarbon fuels are enriched with more than 30% hydrogen, the resulting flames show very different behaviours [8]. This can lead to increased pollution by higher

NO_x emissions. There is also an increased risk of hardware damage of the combustion system. In order to avoid such problems, it is necessary to re-design existing combustion systems. This in turn, necessitates a clear understanding of the behaviour of the flame as the hydrogen content in the fuel mixture is varied.

The aim of the current paper is to advance the understanding of the behaviour of *premixed* flames fuelled with hydrogen or a hydrogen-blend. We consider a laminar flame, which has been extensively studied by earlier authors [9–14]. Its most important parameter is the *laminar flame speed*. This speed plays a crucial role in the interaction of the flame with the velocity field in which the flame resides; it also determines how long or short the flame is. The fuel type and the equivalence ratio of the fuel-air mixture are important parameters that determine the magnitude of the laminar flame speed.

Hydrogen flames have a considerably higher laminar flame speed (around 10 times higher) than conventional hydrocarbon flames. Hydrogen-enriched flames show the same feature, but it is less extreme. This leads to a change in the interaction between the flame and the velocity field, and brings the risk that a feedback loop gets established between unsteady combustion and the acoustic field in the combustion chamber. Such a scenario is the underlying cause of self-sustained large-amplitude periodic pressure oscillations, termed "thermoacoustic instabilities", which can inflict serious mechanical damage to the combustor hardware. Another consequence of their high laminar flame speed is that hydrogen flames are shorter. This brings the risk of another damaging phenomenon, termed "flashback", where the flame moves upstream into the fuel supply line and overheats hardware components that cannot withstand high temperatures.

*Corresponding author

 s.malamal.gopinathan@keele.ac.uk (S.M. Gopinathan);

aswathys@iitm.ac.in (A. Surendran); m.a.heckl@keele.ac.uk (M.A. Heckl)

ORCID(s): 0000-0003-4595-699X (S.M. Gopinathan);

0000-0002-8114-9813 (A. Surendran); 0000-0002-0192-7508 (M.A. Heckl)

List of Symbols

A	velocity amplitude	r	radial position
c	speed of sound	r_p	radius of circular perforation
c_p	specific heat at constant pressure	S	cross-sectional area of tube
\mathcal{F}	Fourier transform	S_L	laminar flame speed (also called laminar burning velocity)
$G(x, x^*, t - t^*)$	Green's function	\bar{T}	mean temperature
\mathcal{G}	scalar field to describe the flame surface	T_{12}, T_{21}	forward and backward transmission coefficients at the interface $x = x_q$
$g_n(x, x^*)$	amplitude of Green's function mode n	$\mathcal{T}(\omega)$	flame transfer function
g_0, g_1	constant coefficients in amplitude-dependence of coupling coefficients	$\mathcal{T}_\varepsilon(\omega)$	flame describing function
H	Heaviside function	t	time
H_f	vertical height of steady flame	u	axial velocity component
$h(t)$	impulse response of the flame's heat release rate (also : time-domain equivalent of $\mathcal{T}(\omega)$)	\bar{u}	mean velocity
$h_\varepsilon(t)$	time-domain equivalent of $\mathcal{T}_\varepsilon(\omega)$	u_m	complex velocity amplitude of thermoacoustic mode m
h_p	thickness of perforated plate	v	radial velocity component
i	imaginary unit	x	axial position
K	heater power per unit mass flow	x_q	axial position of matrix flame
\mathcal{K}	Rayleigh conductivity of perforation	α	half-angle of steady flame
k	wave number	$\varepsilon = A/\bar{u}$	nondimensional velocity amplitude
L	tube length	$\bar{\rho}$	mean density
L_f	side length of steady flame	$\sigma_1, \sigma_2, \sigma_3$	standard deviations of maxima and minimum in impulse response of flame
\mathcal{N}	perforation density, i.e. number of holes per unit area of perforated plate	τ_1, τ_2, τ_3	travel times of maxima and minimum in impulse response of flame
n_1, n_2, n_3	measure of peak values in impulse response of flame	Φ	velocity potential
p'	acoustic pressure	$\varphi_0, \dot{\varphi}_0$	initial values of velocity potential and its gradient
$Q(t)$	heat release rate of the flame	ϕ	equivalence ratio of premix
$q(x, t)$	heat release rate per unit mass of premix	χ_{H_2}	hydrogen concentration
R	base radius of flamelet, radius of perforation	ω	angular frequency
R_0, R_L	reflection coefficients at the tube ends $x = 0$ and $x = L$	ω_n	frequency of mode n of the tailored Green's function
R_{12}, R_{21}	forward and backward reflection coefficients at the interface $x = x_q$	Ω_m	complex eigenfrequency of the thermoacoustic mode m

Overbars denote the mean part of field quantities, primes denote the fluctuating part of field quantities in the time-domain, and hats denote the fluctuating part of field quantities in the frequency-domain. For example, for the heat release rate, the mean part is \bar{Q} , and the fluctuating part is Q' in the time-domain, and \hat{Q} in the frequency-domain.

The time dependence of a quantity oscillating with frequency ω is denoted by $e^{-i\omega t}$.

A landmark experimental study was performed by Dawson's group [15, 16], who measured the flame transfer function (FTF) of a bluff-body-stabilised flame for a range of hydrogen concentrations. They found that an increase of hydrogen in the fuel blend affects the FTF in two ways: it increases the cutoff frequency of the FTF gain and reduces the overall slope of the FTF phase curve. Lim et al. [17] considered a laminar conical flame and predicted the same effects on the FTF; they used a kinematic model for the flame forced by a convected wave with a 2-D velocity field. They found that the influence of the forcing amplitude diminished

with increasing hydrogen concentration. Several papers considered not just the flame dynamics, but a complete combustion system, where a hydrogen-blend flame interacts thermoacoustically with the sound field in an acoustic resonator. These include Karlis et al. [18], who observed dynamic transitions while enriching methane blends with hydrogen in a swirl-stabilised combustor. Similarly, Aguilar et al. [16] observed a series of transitions in the bluff-body stabilised combustor; they subsequently developed a network model, incorporating their FTF, which successfully predicted the transition between two limit cycles.

All previous studies are limited to the frequency-domain in that the flame is modelled with a transfer function. They give no physical insight in terms of the flame dynamics, and more specifically in terms of the disturbance amplitude, hydrogen concentration and equivalence ratio. A time-domain perspective would give such insight because it reveals the travel times of disturbances of the heat release rate; however, this is missing from the literature.

The current paper aims to fill this gap. We will use a time-domain approach to shed light on how the flame responds if it is forced by a velocity field that is representative of premixed laminar combustion test rigs. By considering a large range of velocity amplitudes, we will be able to explain linear and nonlinear effects in the flame dynamics. The most important parameter of the flame dynamics is the laminar flame speed. This is a property of the fuel-air mixture and depends strongly on the hydrogen concentration in the fuel as well as on the equivalence ratio of the mixture. The fundamental insight gained for the flame dynamics is then applied to model a generic combustion test rig with a natural gas - hydrogen flame. The combustion chamber is one-dimensional, and the flame is configured according to the "micromix combustion principle" [19, 20], i.e. a two-dimensional array of small flames is anchored on the downstream side of a perforated plate. From this model, we will calculate the safe operating limits, i.e. the operating conditions (in terms of hydrogen concentration and the equivalence ratio) under which thermoacoustic instabilities and flashback do not occur.

The paper is divided into the following sections. Section 2 describes the combustion system under consideration, in particular the flame and the combustion chamber. Section 3 gives details about the flame model (both in the time-domain and frequency-domain), and predictions are made for the nonlinear flame response. The complete combustion system is modelled in Section 4, adopting a Green's function approach. This is then used in Section 5 to make predictions for safe operating limits; numerical results are presented and discussed. Section 6 lists the main conclusions and makes recommendations for further research.

2. The considered combustion system

We treat the combustion system as a combination of two key elements:

- (1) combustion chamber with a steady flame
- (2) flame in a time-dependent velocity field

The *combustion chamber* is modelled as a quarter-wave resonator with fixed length L . The tube end at $x = 0$ is closed, and the end at $x = L$ is open. At the axial position x_q , there is a jump in mean temperature (due to a steady compact flame there) from \bar{T}_1 to \bar{T}_2 . Also at x_q , there is a perforated plate spanning the cross-section of the resonator tube. We refer to the two regions on either side of x_q as the cold region and the hot region. A schematic illustration of the combustion system is shown in Fig. 1.

One-dimensional acoustic waves travel forwards and backwards in each of the two regions. The tube ends are

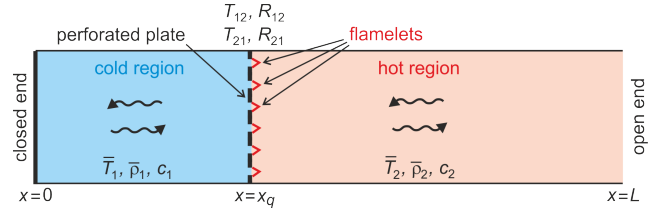


Figure 1: The set-up under consideration. \bar{T} , $\bar{\rho}$ and c are the mean temperature, mean density and speed of sound, respectively; the subscript 1 denotes the cold region, and 2 denotes the hot region.

modelled through their respective reflection coefficients, i.e. $R_0 = 1$ at $x = 0$ and $R_L = -1$ at $x = L$.

At the interface, $x = x_q$, the waves are partly transmitted and partly reflected. We describe this by pressure transmission and reflection coefficients. The pressure transmission coefficients are denoted by T_{12} and T_{21} for a wave approaching from the upstream and downstream section, respectively. The corresponding reflection coefficients are denoted by R_{12} and R_{21} . These coefficients are determined by two elements: the perforated plate and the temperature jump. We model these as individual interfaces, spaced a small distance apart, each with its own reflection and transmission coefficients (see Appendix A). The perforated plate has reflection and transmission coefficients that depend on the following properties: perforation density (\mathcal{N}), radius of perforations (r_p) and plate thickness (h_p); there is also a dependence on frequency. At the temperature jump, the reflection and transmission coefficients are functions of the acoustic impedances $\bar{\rho}_1 c_1$ and $\bar{\rho}_2 c_2$. The two interfaces are lumped together into a single interface at $x = x_q$ by the wave-based approach described in Appendix A.

The combustion chamber will be modelled mathematically in Section 4.2 by the tailored Green's function; this will take into account the perforated plate and the temperature jump.

The *flame* is modelled as a matrix flame, i.e. it is made up of a two-dimensional array of small flamelets, each anchored at the circular downstream edge of a perforation (see Fig. 1). The flamelets are assumed to be identical and non-interacting. Each is laminar and conical with base radius R . They are fed by a blend of hydrogen and natural gas, premixed with air. The premix is characterised by its equivalence ratio ϕ and by the hydrogen concentration χ_{H_2} .

The matrix flame is situated in the near-field of the perforated plate, where the velocity field has two components: an axial and a radial component; both vary with time and thus distort the surface of each flamelet. This is illustrated by the snapshot in Fig. 2. The velocity field is marked by small black arrows, and the flame surface is marked by a red curve. This flame will be modelled in Section 3 with a kinematic approach (level-set method).

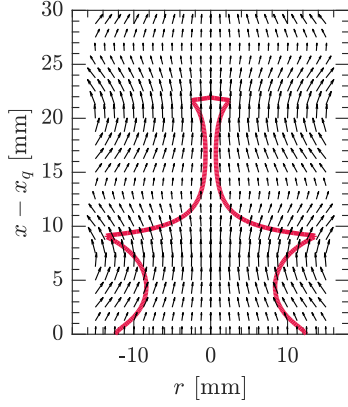


Figure 2: Conical flame in a velocity field. Arrows \rightarrow indicate the velocity field; the red curve --- indicates the flame surface.

3. Model for the flame

We consider only fluctuations in velocity (but not in equivalence ratio); also the effect of the flame curvature on the laminar flame speed S_L is neglected. In Section 3.1, we describe the response of the flame to harmonic perturbations of a given frequency, and in Section 3.2, we take a time-domain perspective. The model we use for flashback is presented in Section 3.3.

3.1. Flame model in terms of the flame describing function

We consider each flamelet as a conical laminar flame, which forms an interface separating the unburnt mixture from the burnt mixture. This interface, which is called the flame front, adjusts its shape to the velocity field in such a way that the flame-normal velocity component is equal to the laminar flame speed S_L . This kinematic balance is described by the G-equation [21]

$$\frac{\partial \mathcal{G}}{\partial t} + u \frac{\partial \mathcal{G}}{\partial x} + v \frac{\partial \mathcal{G}}{\partial r} = S_L \sqrt{\left(\frac{\partial \mathcal{G}}{\partial x}\right)^2 + \left(\frac{\partial \mathcal{G}}{\partial r}\right)^2}, \quad (1)$$

where \mathcal{G} is a scalar field that defines the instantaneous position of the flame surface: $\mathcal{G} < 0$ in the unburnt mixture, $\mathcal{G} > 0$ in the burnt mixture, and $\mathcal{G} = 0$ at the flame surface. u and v are the (time-dependent) axial and radial velocity components at a point on the flame surface, and S_L is constant. The schematic in Fig. 3 shows a perturbed flame surface, and also the notation to describe it mathematically.

Equation (1) is a nonlinear PDE; we solve it numerically with the level-set solver GFlame [22, 23]. For the boundary conditions, we assume that the flame is fixed at the flame base (i.e. at $x = 0$). The flame is forced by a velocity field, which we describe by Cuquel's 2-D incompressible convective velocity model [24, Chapter 4]. The axial component of the velocity field has a mean part \bar{u} and a harmonic perturbation part with frequency ω and amplitude $\bar{u}\epsilon$,

$$u(x, t) = \bar{u} \left[1 + \epsilon \sin(\omega t - \frac{\omega}{\bar{u}} x) \right], \quad (2)$$

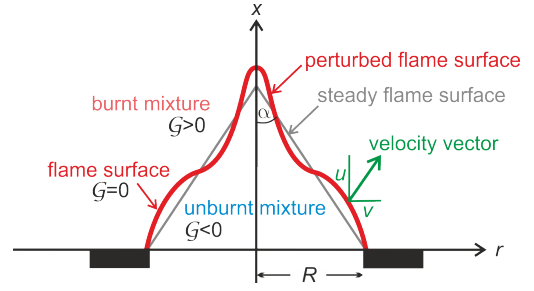


Figure 3: Schematic of a conical flame. --- steady flame; --- perturbed flame. α is the half-angle of the steady flame; it is given by $\sin \alpha = S_L / \bar{u}$, where \bar{u} is the mean of u .

while the radial component of the velocity field is purely oscillatory and given by

$$v(x, r, t) = r \omega \epsilon \cos(\omega t - \frac{\omega}{\bar{u}} x) \quad (3)$$

(to satisfy the continuity equation for incompressible flow).

GFlame calculates the instantaneous flame shape, and from that the instantaneous flame surface area. The heat release rate is obtained by assuming that it is proportional to the flame surface area [9]. After a sufficient number of time steps, the time history of $Q'(t)$ (fluctuating part of the heat release rate) is obtained. This is equivalent to $\hat{Q}(\omega)$, which is the heat release rate in the frequency domain. By performing a frequency sweep, $\hat{Q}(\omega)$ is obtained for a range of frequencies.

The matrix flame is a composite of N individual flamelets, where N is the number of holes in the perforated plate that anchors the flame. Therefore, the heat release rate from the whole matrix flame is N times that of an individual flamelet: $NQ'(t)$ and $N\hat{Q}(\omega)$ are the fluctuating heat release rate in the time domain and frequency domain, respectively, and $N\bar{Q}$ is the mean heat release rate of the matrix flame, where \bar{Q} is the mean heat release rate of an individual flamelet (calculated by GFlame).

The forced flame can be regarded as an input-output system, where the velocity field is the input and the heat release rate is the output. It can be described in the frequency domain by the "flame transfer function" (FTF), which we denote by $\mathcal{T}(\omega)$. The FTF is defined by the quotient

$$\mathcal{T}(\omega) = \frac{\hat{Q}(\omega) / \bar{Q}}{\hat{u}(\omega) / \bar{u}}. \quad (4)$$

$\hat{u}(\omega)$ is the axial component of the velocity at the flame base in the frequency-domain; it is normalised by the mean velocity \bar{u} .

For very small perturbations of the flame surface, the FTF is assumed to be independent of the amplitude of the imposed velocity. For larger perturbations, the FTF becomes amplitude-dependent. In such a case the transfer function is termed "flame describing function" (FDF) and written as [25]

$$\mathcal{T}_\epsilon(\omega) = \frac{\hat{Q}(\omega, \epsilon) / \bar{Q}}{\hat{u}(\omega) / \bar{u}}, \quad (5)$$

Table 1
Parameters describing the flame

Parameter	Symbol	Numerical value	Units
flame base radius	R	0.001	m
mean velocity	\bar{u}	1	ms^{-1}
laminar flame speed	S_L	0.411 and 0.557	ms^{-1}
amplitude of the velocity that forces the flame	$\varepsilon = A/\bar{u}$	0.02 ... 0.4	-

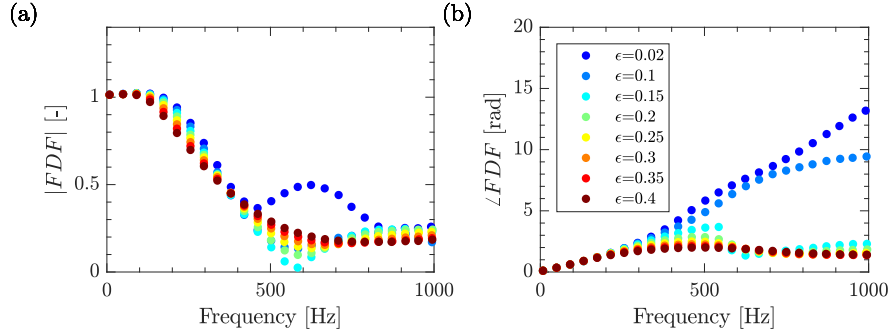


Figure 4: FDF for a conical flame with $S_L = 0.411 \text{ ms}^{-1}$; (a) gain; (b) phase.

where ε is the nondimensional form of the amplitude A of the velocity fluctuations $u'(t)$,

$$A = \bar{u}\varepsilon. \quad (6)$$

We calculate the FDF by running GFlame for a range of excitation amplitudes. The flame parameters used in the calculation are shown in Table 1.

A sample of results can be seen in Figs. 4 and 5 for a small conical flame. Figure 4 shows the amplitude dependence for a small flame speed ($S_L = 0.411 \text{ ms}^{-1}$), and Fig. 5 shows it for a larger flame speed ($S_L = 0.557 \text{ ms}^{-1}$). Parts (a) of the two figures give the gain, $|\mathcal{T}_\varepsilon(\omega)|$, of the FDF, and parts (b) give the phase, $\angle\mathcal{T}_\varepsilon(\omega)$.

Figures 4 and 5 show very clearly that the FDF depends on the amplitude of the imposed velocity field, as well as on the laminar flame speed. In particular, we observe that for the higher S_L -value, the cut-off frequency in the gain (IFDF) is larger, and the slope of the phase curve ($\angle\text{FDF}$) is smaller at low frequencies. Both observations are consistent with those reported in [17]. We further observe that the phase curve levels off at higher frequencies as the forcing amplitude increases. This is in line with the experimental results obtained by Karimi et al. [26].

3.2. Flame model in the time-domain

The Rayleigh index, which is the time average $\overline{Q'(t)p'(t)}$, where $p'(t)$ is the acoustic pressure at the flame, is a key indicator for thermoacoustic instabilities [27, 28]. It depends critically on the phase difference between $Q'(t)$ and $p'(t)$, which in turn depends strongly on any time-lags between the heat release rate and the acoustic field. This is our motivation for taking a time-domain perspective and transforming the results of the previous section into the time-domain.

3.2.1. Linear flame model

The impulse response of the flame is the time history of the heat release rate oscillations triggered by a velocity impulse [23, Eq. (2.6)]; we denote it by $h(t)$. It is the time-domain equivalent of the FTF, $\mathcal{T}(\omega)$; in fact $h(t)$ and $\mathcal{T}(\omega)$ form a Fourier transform pair,

$$h(t) = \mathcal{F}^{-1}[\mathcal{T}(\omega)], \quad (7)$$

where \mathcal{F}^{-1} denotes the inverse Fourier transform. The heat release rate $Q'(t)$ can be expressed in terms of $h(t)$ by

$$\frac{Q'(t)}{\bar{Q}} = \int_{\tau=0}^t h(\tau) \frac{u'(t-\tau)}{\bar{u}} d\tau. \quad (8)$$

The impulse response is a linear concept, so it is only valid at very small amplitudes, such as $\varepsilon = 0.02$ [29]. We calculated it for a range of S_L -values between 0.41 and 0.56 ms^{-1} . The results can be seen in Fig. 6.

We observe from Fig. 6 that the impulse response has a minor maximum in the early part of the time-history; this is followed by a major maximum and then a minimum. Partial insight into these features can be gained from the studies in Blumenthal et al. [12] and Steinbacher [23]. They calculated the analytical solution for the impulse response from the linearised G-equation. This revealed two travel times: a "convection time" Δt_c and a "restoration time" Δt_r . The convection time is the time it takes for a velocity perturbation to travel along the flame axis from the base to the tip of the flame; it is given by

$$\Delta t_c = \frac{H_f}{\bar{u}}, \quad (9)$$

where $H_f = (R/\tan \alpha)$ is the vertical height of the steady flame.

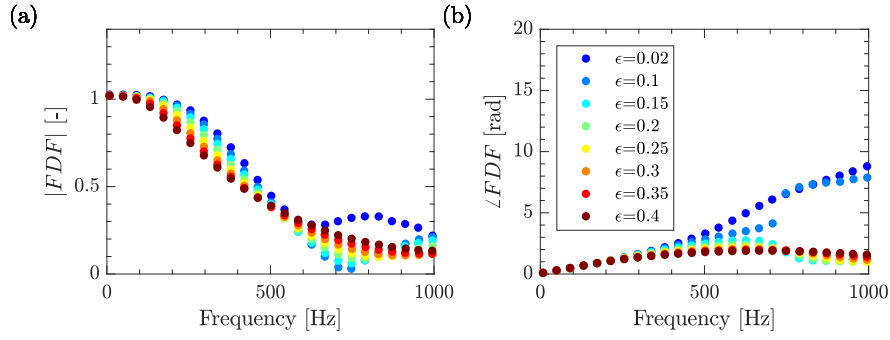


Figure 5: FDF for a conical flame with $S_L = 0.557 \text{ ms}^{-1}$; (a) gain; (b) phase.

Table 2
Comparison of travel times

$S_L [\text{ms}^{-1}]$	α	$H_f [m]$	$L_f [m]$	$\tau_1 [s]$ from Fig.6	$\tau_2 [s]$ from Fig.6	$\Delta t_c [s]$ from Eq.(9)	$\tau_3 [s]$ from Fig.6	$\Delta t_r [s]$ from Eq.(10)
0.41	0.42	0.0022	0.0025	0.0008	0.0018	0.0022	0.0026	0.0026
0.43	0.44	0.0021	0.0023	0.0007	0.0017	0.0021	0.0025	0.0026
0.46	0.48	0.0019	0.0022	0.0006	0.0016	0.0019	0.0024	0.0024
0.50	0.52	0.0017	0.0020	0.0005	0.0014	0.0017	0.0022	0.0023
0.56	0.59	0.0015	0.0018	-	0.0013	0.0015	0.0021	0.0022

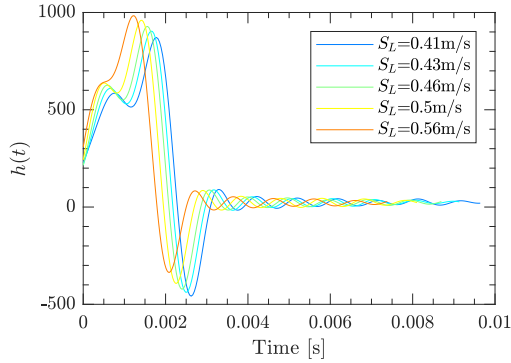


Figure 6: Impulse response $h(t)$ of flames with different laminar flame speeds excited by a low-amplitude acoustic field with $\epsilon = 0.02$.

The restoration time is the time it takes for the flame to restore its unperturbed shape after a perturbation has passed; it is given by

$$\Delta t_r = \frac{L_f}{u_{\parallel}}, \quad (10)$$

where $L_f = (H_f / \cos \alpha)$ is the side length of the steady flame, and $u_{\parallel} = \bar{u} \cos \alpha$ is the component of the mean velocity \bar{u} that is parallel to the steady flame surface.

Table 2 lists these travel times, together with the positions along the time-axis of the minor maximum (τ_1), major maximum (τ_2) and minimum (τ_3) of the time histories in Fig. 6. These positions are in sequence, i.e. τ_1 is the shortest and τ_3 the longest travel time.

Comparison of columns 6 and 7 shows that the major maximum at τ_2 corresponds to the convection time Δt_c ; comparison of columns 8 and 9 shows that the minimum at τ_3 corresponds to the restoration time Δt_r . There are slight discrepancies, but this is to be expected: Blumenthal et al. [12] linearised the G-equation and considered a purely axial velocity field, whereas we solved the fully *nonlinear* G-equation and considered a velocity field with an axial *and* radial component. Furthermore, we observe from our results that τ_2 and τ_3 reduce as S_L increases and the flame becomes shorter.

The minor maximum in the early part of the impulse response shown in Fig. 6 (with time-lag τ_1 listed in column 5 of Table 2) is not captured by the Blumenthal model. The values of τ_1 reduce at a similar rate as τ_2 and τ_3 when S_L increases. We therefore hypothesise that the minor maximum is due to a nonlinear effect, which occurs even at very small velocity amplitudes, and that it is caused by some propagation process. The minor maximum is more prominent for long flames than for short ones.

We now proceed to quantify the changes in the impulse response curves due to changes in S_L . Motivated by the shape of these curves, we approximate them analytically by a superposition of three Gauss curves,

$$h(t) = n_1 D_1(\tau - \tau_1) + n_2 D_2(\tau - \tau_2) + n_3 D_3(\tau - \tau_3), \quad (11a)$$

with distributions

$$D_j(\tau - \tau_j) = \frac{1}{\sigma_j \sqrt{2\pi}} \exp\left(-\frac{(\tau - \tau_j)^2}{2\sigma_j^2}\right), \quad j = 1, 2, 3 \quad (11b)$$

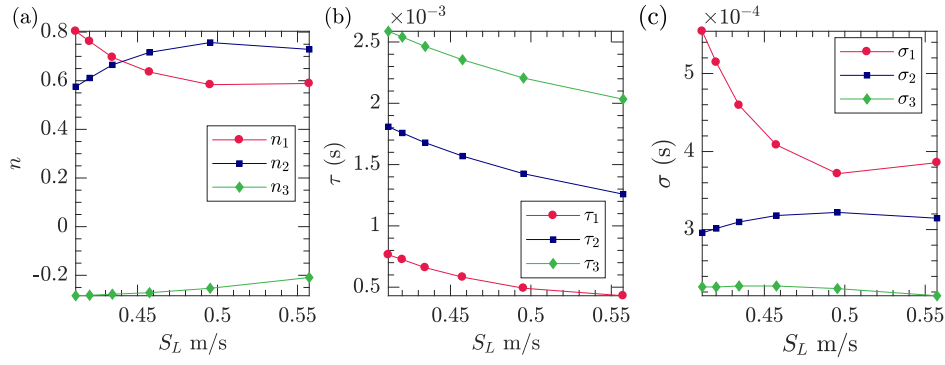


Figure 7: Dependence of the fitting parameters on the laminar flame speed S_L . (a) n_1, n_2, n_3 ; (b) τ_1, τ_2, τ_3 ; (c) $\sigma_1, \sigma_2, \sigma_3$.

n_1 and n_2 are a measure for the peak value of the first two maxima; n_3 is associated with the minimum and is negative. τ_j ($j = 1, 2, 3$) is the central time-lag of distribution j , and σ_j ($j = 1, 2, 3$) is the standard deviation. The quantities $n_1, n_2, n_3, \tau_1, \tau_2, \tau_3, \sigma_1, \sigma_2, \sigma_3$ are treated as fitting parameters, and they are determined in the frequency-domain as described in [30]. They depend on S_L as shown in Fig. 7. The features that can be observed from the curves in Fig. 7 are fully in line with the results in Fig. 6, and give further insight:

- (1) With increasing S_L , the three times τ_1, τ_2, τ_3 decrease monotonically. This is expected because an increase in S_L leads to a shortening of the flame and therefore to reduced travel times.
- (2) With increasing S_L , n_1 decreases, while n_2 increases. However, the ratios n_1/σ_1 and n_2/σ_2 , which are a measure for the peak values of the two maxima, increase steadily – in line with the trend of the two maxima seen in Fig. 6. The parameter n_3 is negative, as expected for the minimum. The modulus of the ratio n_3/σ_3 reduces with increasing S_L , and this reflects the trend of the minimum in Fig. 6, which becomes shallower.
- (3) The values of $\sigma_1, \sigma_2, \sigma_3$ are a measure for the width of the maxima and minimum. σ_1 decreases with S_L , indicating that the first maximum becomes narrower; σ_2 and σ_3 barely change, along with the width of the second maximum and the minimum.

3.2.2. Amplitude-dependent flame model

We now consider an *amplitude-dependent* flame response described by an FDF. If we apply an inverse Fourier transform to the FDF, we obtain a time-domain signal, but its interpretation as "impulse response" is no longer valid [29]. Nevertheless, the transform can be performed; we call the resulting signal the "time-domain equivalent of the FDF" and denote it by $h_\varepsilon(t)$. Fig. 8 shows the time-domain results corresponding to the FDFs in Figs. 4 and 5. Figure 8(a) is for the long flame ($S_L = 0.411 \text{ ms}^{-1}$), and Fig. 8(b) is for the short flame ($S_L = 0.557 \text{ ms}^{-1}$).

We make the following observations from Fig. 8(a). The first maximum grows as ε increases, while its position remains largely unchanged. The second maximum reduces

in height as ε increases, and its position shifts to the left. Eventually, it merges with the earlier maximum, which becomes the dominant one. The minimum becomes shallower as ε increases, and soon disappears altogether; its position seems to shift slightly to the left. The shorter flame shows similar trends (see Fig. 8(b)), but these are harder to discern.

In order to quantify how the curves in Fig. 8 change as ε increases, we represent them again by a superposition of three Gauss curves with fitting parameters $n_1, n_2, n_3, \tau_1, \tau_2, \tau_3, \sigma_1, \sigma_2, \sigma_3$. Figure 9 shows the fitting parameters for the long flame ($S_L = 0.411 \text{ ms}^{-1}$), and Fig. 10 shows them for the short flame ($S_L = 0.557 \text{ ms}^{-1}$).

The results in Figs. 9 and 10 confirm the observations made from Figs. 8(a) and 8(b), respectively. We start by analysing the results in Fig. 9 with reference to Fig. 8(a). The first maximum is described by the parameters n_1, τ_1, σ_1 . As ε increases beyond the value 0.2, n_1 increases, while τ_1 and σ_1 remain largely constant. Hence, the ratio n_1/σ_1 , which is a measure for the peak value of the maximum, increases. The second maximum is described by the parameters n_2, τ_2, σ_2 . As ε increases beyond the value 0.2, n_2 and τ_2 decrease, while σ_2 increases at first and then levels off. The movement of this maximum to the left along the time axis in Fig. 8(a) corresponds to the decrease in τ_2 . The loss of height of this maximum is reflected by the decrease of the ratio n_2/σ_2 . The minimum is described by the parameters n_3, τ_3, σ_3 . As ε increases, n_3 tends monotonically to zero. This implies that the minimum is disappearing and therefore the values for τ_3 and σ_3 become meaningless. We conclude from the disappearance of the minimum that the flame restoration process fades with increasing excitation amplitude. Qualitatively similar observations can be made from the results for the short flame shown in Fig. 10, and the corresponding time histories in Fig. 8(b).

The existence of two maxima with two different travel times, τ_1 and τ_2 , implies that two different travel *distances* are at play here. In order to shed more light on this, we investigate the flame kinematics from snapshots of the flame surface taken at different times during one oscillation cycle. This is illustrated in the two figures below, for an excitation with a frequency of $f = 400 \text{ Hz}$ and three different amplitudes ($\varepsilon = 0.02, 0.10, 0.40$). Figure 11 is for a long flame

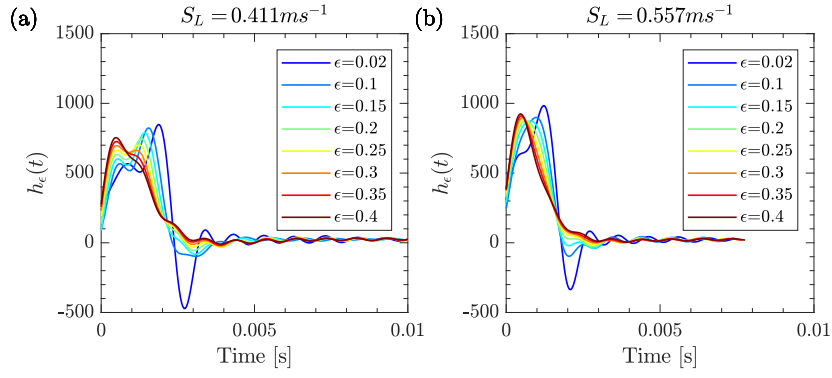


Figure 8: "Time-domain equivalents" corresponding to the FDFs in Figs. 4 and 5 for different excitation amplitudes ϵ ; (a) $S_L = 0.411 \text{ ms}^{-1}$, corresponding to Fig. 4; (b) $S_L = 0.557 \text{ ms}^{-1}$, corresponding to Fig. 5.

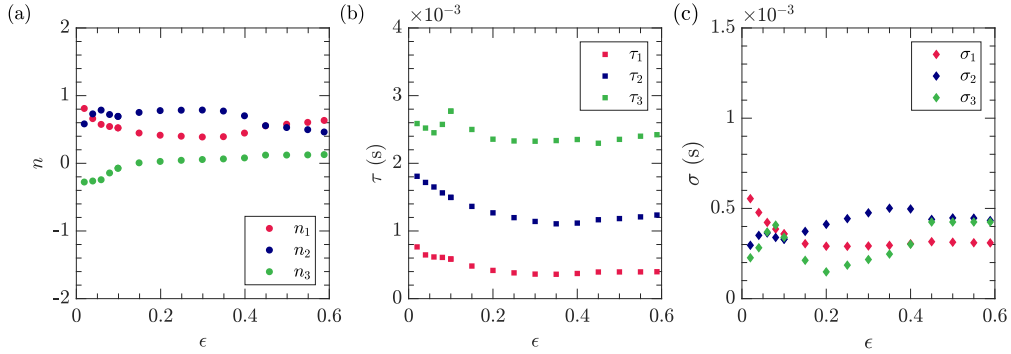


Figure 9: Amplitude-dependence of the fitting parameters for small S_L ($S_L = 0.411 \text{ ms}^{-1}$). (a) n_1, n_2, n_3 ; (b) τ_1, τ_2, τ_3 ; (c) $\sigma_1, \sigma_2, \sigma_3$. The step size for ϵ is 0.02 for $\epsilon \leq 0.1$ and 0.05 for $\epsilon > 0.1$.

with $S_L = 0.411 \text{ ms}^{-1}$, and Fig. 12 is for a short flame with $S_L = 0.557 \text{ ms}^{-1}$. In both figures, the height of the steady flame H_f is marked by a grey horizontal line.

We first consider the long flame. Figure 11(a) shows the flame movement for the very low excitation amplitude $\epsilon = 0.02$, which was considered previously (see Section 3.2.1) as a linear case. Careful examination of the displayed snapshots shows that the flame tip oscillates around a position, which is below the position of the steady flame tip. The flame response to higher excitation amplitudes is shown in the subsequent parts of Fig. 11: the case $\epsilon = 0.10$ is in part

(b), and the case $\epsilon = 0.40$ is in part (c). It is evident that the flame tip oscillates around a lower and lower mean as ϵ increases. Effectively, the mean flame height reduces, so the convection time Δt_c identified in the previous section (see Eq. (9)) becomes shorter. This is the reason for the shift to smaller τ_2 -values as ϵ increases (see Fig. 9(b)). It is a nonlinear phenomenon, which occurs even for very small excitation amplitudes.

The snapshots for $\epsilon = 0.40$ (see Fig. 11(c)) reveal that flame pinching occurs. This leads to a substantial reduction of the effective mean height of the flame. We hypothesise

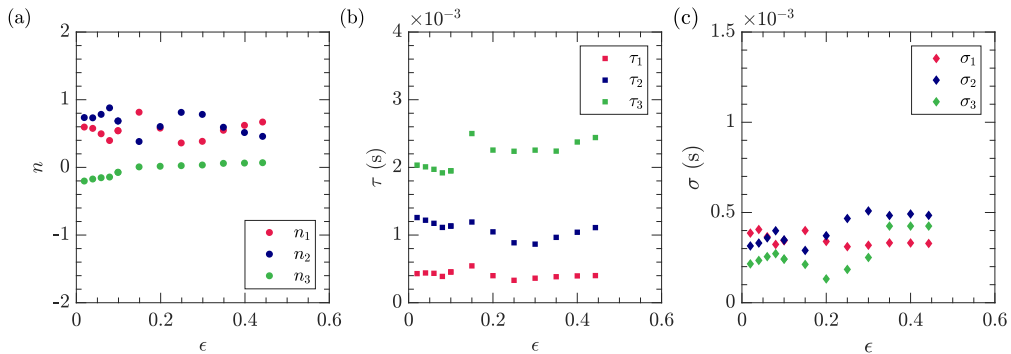


Figure 10: Amplitude-dependence of the fitting parameters for large S_L ($S_L = 0.557 \text{ ms}^{-1}$). (a) n_1, n_2, n_3 ; (b) τ_1, τ_2, τ_3 ; (c) $\sigma_1, \sigma_2, \sigma_3$. The step size for ϵ is 0.02 for $\epsilon \leq 0.1$ and 0.05 for $\epsilon > 0.1$.

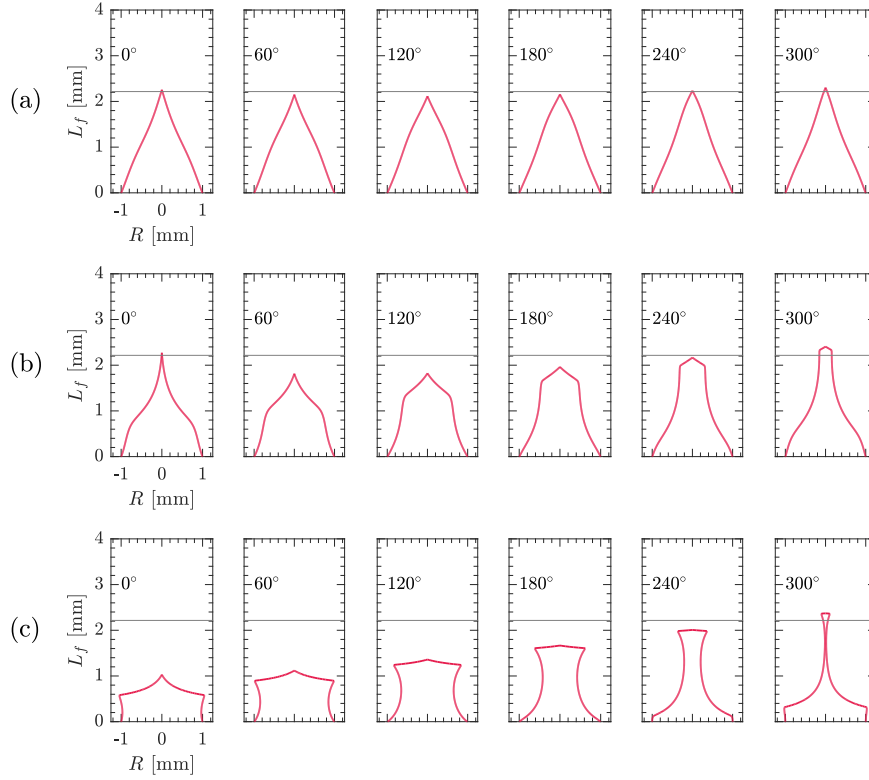


Figure 11: Snapshots of the flame surface in cross-section at 6 time instances during one cycle for $f = 400\text{Hz}$ and $S_L = 0.411\text{ms}^{-1}$. The grey horizontal line marks the height of the corresponding steady flame. (a) $\varepsilon = 0.02$; (b) $\varepsilon = 0.10$; (c) $\varepsilon = 0.40$.

that this is the reason why the early maximum at τ_1 becomes the dominant maximum as ε increases.

Much the same observations can be made for the short flame (see Fig. 12), but they are harder to discern.

In summary, we can conclude that two kinematic phenomena occur as ε increases:

- (1) The mean height of the oscillating flame decreases progressively and is always below the height of the steady flame (even for very small excitation amplitudes).
- (2) Flame pinching is responsible for a substantial reduction in the mean flame height. It suppresses the former phenomenon and leads to an increasingly dominant maximum (at τ_1) early on in the time history of the impulse response.

These phenomena cannot always be separated, especially for short flames.

3.3. Flame flashback

Flashback is the phenomenon of the flame (or part of the flame) moving upstream into the premix supply line. It cannot occur if the velocity of the incoming premix exceeds the laminar flame speed, i.e. if $\bar{u} + u'(x, t) > S_L$. $u'(x, t)$ has amplitude $\bar{u}\varepsilon$, so the minimum of $u'(x, t)$ is $-\bar{u}\varepsilon$ (see Eq. (2)). Therefore, the limiting amplitude, $\bar{u}\varepsilon_f$, where flashback is

guaranteed to be absent is given by $\bar{u} - \bar{u}\varepsilon_f = S_L$, or [31]

$$\varepsilon_f = 1 - \frac{S_L}{\bar{u}}. \quad (12)$$

4. Model for the complete combustion system

We now consider the complete combustion system shown in Fig. 1.

4.1. Model in terms of PDE, boundary conditions and initial conditions

The 1-D acoustic analogy equation

$$\frac{1}{c^2} \frac{\partial^2 \Phi}{\partial t^2} - \frac{\partial^2 \Phi}{\partial x^2} = -\frac{\gamma - 1}{c^2} q(x, t) \quad (13)$$

is the governing equation for the acoustic field in a tube with a distributed heat release rate [32]. $\Phi(x, t)$ is the velocity potential, and $q(x, t)$ is the heat release rate of the matrix flame per unit mass of the premix. Any mean flow through the tube is neglected in the acoustic waves. In addition to this PDE, $\Phi(x, t)$ also has to satisfy

- initial conditions given at $t = 0$ for Φ and $\frac{\partial \Phi}{\partial t}$
- boundary conditions at the tube ends $x = 0, L$

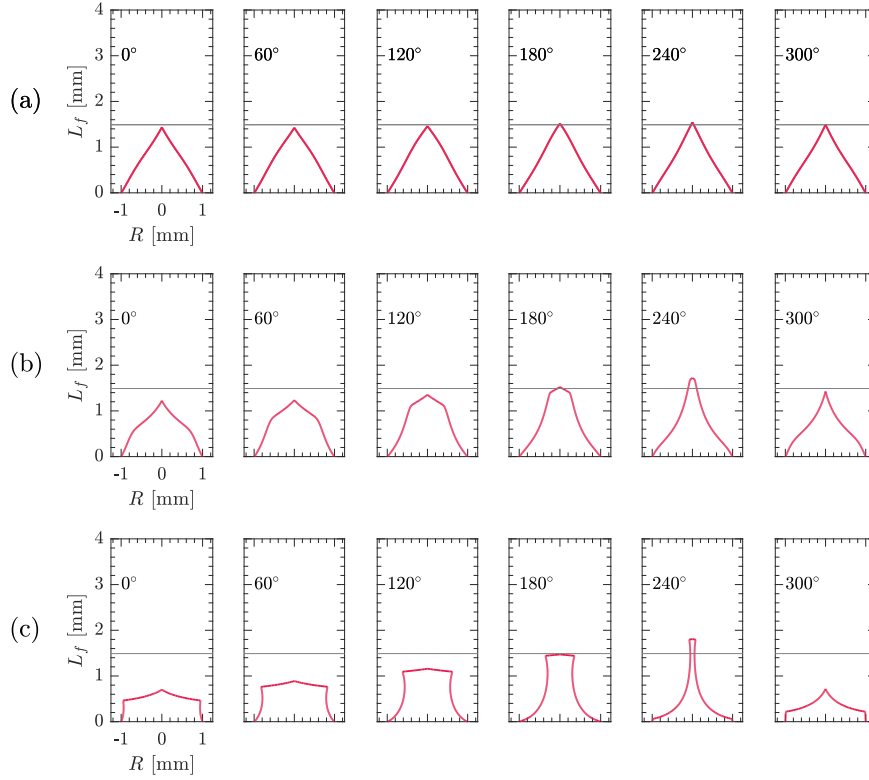


Figure 12: Snapshots of the flame surface in cross-section at 6 time instances during one cycle for $f = 400\text{Hz}$ and $S_L = 0.557\text{ms}^{-1}$. The grey horizontal line marks the height of the corresponding steady flame. (a) $\varepsilon = 0.02$; (b) $\varepsilon = 0.10$; (c) $\varepsilon = 0.40$.

- conditions at $x = x_q$ to describe the perforated plate and the temperature jump.

We assume that the flame is compact, and that the heat release rate is concentrated at the axial position x_q . Then we can put

$$q(x, t) = q(t)\delta(x - x_q). \quad (14)$$

The term $q(t)$ is a measure of the global heat release rate $Q'_m(t)$ of the matrix flame,

$$Q'_m(t) = \int_V q'(x, t)\bar{\rho} dV = \bar{\rho}S q(t), \quad (15)$$

where V is a control volume surrounding the flame and S is the cross-sectional area of the tube.

We assume that the initial conditions act at the same position x_q (and nowhere else) and describe them by

$$\Phi(x, t)|_{t=0} = \varphi_0\delta(x - x_q), \quad (16a)$$

$$\frac{\partial\Phi(x, t)}{\partial t}|_{t=0} = \dot{\varphi}_0\delta(x - x_q), \quad (16b)$$

where φ_0 and $\dot{\varphi}_0$ are the initial values of the velocity potential and its gradient. The boundary conditions are

$$\frac{\partial\Phi(x, t)}{\partial x}|_{x=0} = 0 \quad (\text{closed end}), \quad (17a)$$

$$\Phi(x, t)|_{x=L} = 0 \quad (\text{open end}). \quad (17b)$$

The conditions at $x = x_q$ (perforated plate and temperature jump) were modelled with the reflection and transmission coefficients $R_{12}, T_{12}, R_{21}, T_{21}$ spelled out in Appendix A.

Equations (13) to (17b), together with (A.9) and (A.10), fully describe the acoustic field in the tube with thermoacoustic feedback. However, they are not easy to solve, and therefore we resort to a more achievable, but equivalent, approach.

4.2. Model in terms of an integral equation based on the tailored Green's function

The Green's function $G(x, x^*, t - t^*)$ is the response observed at position x and time t to a hypothetical point source at position x^* firing an impulse at time t^* . Its governing equation is

$$\frac{1}{c^2} \frac{\partial^2 G}{\partial t^2} - \frac{\partial^2 G}{\partial x^2} = \delta(x - x^*)\delta(t - t^*). \quad (18)$$

The *tailored* Green's function [33] is the solution of Eq. (18), which satisfies the same conditions at all boundaries and interfaces as the acoustic field (here expressed in terms of the velocity potential). Given that the tube is a resonator, the tailored Green's function is a superposition of modes,

$$G(x, x^*, t-t^*) = H(t-t^*) \operatorname{Re} \left[\sum_{n=1}^{\infty} g_n(x, x^*) e^{-i\omega_n(t-t^*)} \right]. \quad (19)$$

$H(t-t^*)$ stands for the Heaviside function; it guarantees causality. Mode n has frequency ω_n and amplitude g_n . These properties can be calculated analytically [34] (where details of the calculation are described for a similar 1-D setup) and the results are

$$g_n(x, x^*) = \frac{i\hat{g}(x, x^*, \omega_n)}{\omega_n F'(\omega_n)} \quad (20)$$

where F' denotes the derivative of F with respect to ω , and

$$\hat{g}(x, x^*, \omega_n) = \begin{cases} A(x, \omega)C(x^*, \omega) & \text{for } 0 \leq x < x_q \\ C(x^*, \omega)D(x, \omega) & \text{for } x_q \leq x \leq x^* \\ C(x, \omega)D(x^*, \omega) & \text{for } x^* \leq x \leq L \end{cases} \quad (21)$$

with

$$A(x, \omega) = T_{21} [R_0 e^{ik_1 x} + e^{-ik_1 x}], \quad (22)$$

$$C(x, \omega) = ic_2 e^{ik_2(x_q-L)} e^{ik_2(x-x_q)} \times [1 + R_L e^{-2ik_2(x-L)}], \quad (23)$$

$$D(x, \omega) = [e^{-ik_1 x_q} - R_0 R_{12} e^{ik_1 x_q}] \times [e^{-ik_2(x-x_q)} + R_{21} e^{ik_2(x-x_q)}] + R_0 T_{12} T_{21} e^{ik_2 x_q} e^{ik_2(x-x_q)}. \quad (24)$$

The characteristic equation for ω_n is

$$F(\omega) = -e^{-i\omega b} + R_L R_{21} e^{-i\omega a} + R_0 R_{12} e^{i\omega a} - R_0 R_L (R_{12} R_{21} - T_{12} T_{21}) e^{i\omega b}, \quad (25)$$

where

$$a = \frac{x_q}{c_1} + \frac{x_q}{c_2} - \frac{L}{c_2} \quad \text{and} \quad b = \frac{x_q}{c_1} - \frac{x_q}{c_2} + \frac{L}{c_2}. \quad (26a,b)$$

The tailored Green's function offers an alternative to solving the mathematical problem described in Section 4.1 in that it facilitates conversion of the PDE, Eq. (13), together with all boundary conditions and interface conditions, into an *integral equation*. This involves several mathematical steps, which can be found in [32, Section 3]. The result is

$$u'_q(t) = -\frac{\gamma-1}{c^2} \int_{t^*=0}^t H(t-t^*) \operatorname{Re} \left[\sum_{n=1}^{\infty} G_n e^{-i\omega_n(t-t^*)} \right] q(t^*) dt^*$$

$$- \frac{1}{c^2} \operatorname{Re} \left[\sum_{n=1}^{\infty} G_n e^{-i\omega_n t} (i\omega_n \varphi_0 - \dot{\varphi}_0) \right], \quad (27)$$

where $u'_q(t)$ is the time-history of the acoustic velocity at the point $x = x_q$, and G_n is given by

$$G_n = \left. \frac{\partial g_n}{\partial x} \right|_{\substack{x = x_q \\ x^* = x_q}}. \quad (28)$$

The integral on the right-hand side of Eq. (27) gives the velocity field generated by the thermoacoustic interaction. The other terms on the right-hand side are due to the initial conditions given by Eq. (16). In order to determine $q(t)$ for a given FDF $\mathcal{T}_\varepsilon(\omega)$, we use Eq. (7) to calculate the corresponding time-domain equivalent $h_\varepsilon(t)$, Eq. (8) to calculate $Q'_m(t)$ and finally Eq. (15) to get $q(t)$. The integral equation Eq. (27) can be solved with a straightforward time-stepping iteration. We choose the initial amplitude ε by adjusting the initial value φ_0 in Eq. (16a), and we put $\dot{\varphi}_0 = 0$ throughout.

We supplement the time-history calculations with another analytical method, which gives the complex eigenfrequencies of the complete thermoacoustic system. In this model, the acoustic velocity is expressed as a sum of modes with complex amplitudes u_m and complex eigenfrequencies Ω_m ,

$$u'_q(t) = \sum_{m=1}^{\infty} \left(u_m e^{-i\Omega_m t} + \tilde{u}_m e^{i\tilde{\Omega}_m t} \right); \quad (29)$$

the tilde \sim denotes complex conjugates. The real part of Ω_m represents the oscillation frequency, and the imaginary part gives the growth rate, which is an indicator of instability. Bigongiari and Heckl [35] derived equations for Ω_m and u_m , assuming a basic heat release model with a single time-lag.

We extend this approach to the heat release model presented in Section 3.2 in terms of a *distribution* of time lags. Details of the calculation can be found in Appendix B. The resulting equation for Ω_m is

$$\int_{\tau=0}^{\infty} h_\varepsilon(\tau) e^{i\Omega_m \tau} d\tau \sum_{n=1}^{\infty} \left[\frac{G_n}{i(\omega_n - \Omega_m)} - \frac{\tilde{G}_n}{i(\tilde{\omega}_n + \Omega_m)} \right] = -\frac{2c^2}{K(\gamma-1)}; \quad (30)$$

we adopt this in the next section to make stability predictions.

5. Predictions for safe operation limits

Thermoacoustic instabilities, as well as flashback, impose limits on the parameter range, in which safe operation of the combustion system is possible. Both phenomena depend strongly on the laminar flame speed, which in turn depends strongly on the hydrogen concentration χ_{H_2} in the fuel blend and the equivalence ratio ϕ of the fuel-air mix. This dependence is described in Section 5.1. An overall

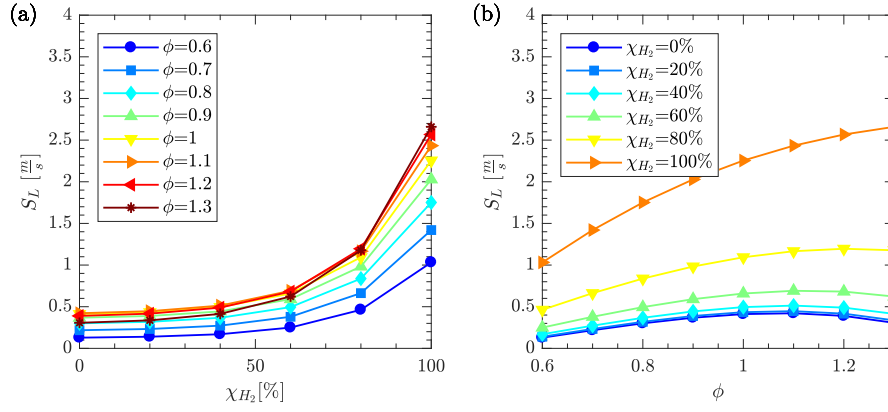


Figure 13: Variation of the laminar flame speed with respect to (a) χ_{H_2} and (b) ϕ [36].

stability map in the 3-D parameter space, made up of χ_{H_2} , ϕ and the velocity amplitude ε , will be given in Section 5.2. Section 5.3 focuses on the parameters χ_{H_2} and ϕ individually, and their influence on the stability behaviour.

5.1. The laminar flame speed for hydrogen-blend fuels

The primary parameter of the flame that characterises its response is the laminar flame speed S_L . For hydrogen-blend flames, S_L depends on the hydrogen concentration, χ_{H_2} and the equivalence ratio ϕ . This dependence is shown in Figs. 13(a) and (b).

It is evident that S_L depends very strongly on χ_{H_2} : it increases by a factor of about 10 (from 0.1 to 1 m/s) for $\phi = 0.6$ as χ_{H_2} increases from 0 to 100%. For other ϕ -values, the increase is in the same ball park.

5.2. Stability-flashback map in 3-D parameter space

Our parameters of interest are

- χ_{H_2} , which we vary in the range [0 ... 70%], step size: 10%
- ϕ , which we vary in the range [0.85 ... 1.3], step size: 0.05
- ε , for which we assume the values 0.02, 0.10, 0.15 ... 0.85; the step size is 0.05 for $\varepsilon \geq 0.1$.

The flame is a matrix flame, i.e. it consists of a 2-D array of small flames anchored on a perforated plate. Each of these small flames has the same base radius and mean velocity as the flame analysed in Section 3.1 (see Table 1). The other system parameters, which are kept constant, are listed in Table 3.

The temperature \bar{T}_2 in the hot region depends on the composition of the premix. We take \bar{T}_2 to be equal to the adiabatic flame temperature and determine it, using the NASA CEA computer program [37, 38]. The mean heat release rate \bar{Q}_m of the matrix flame is then calculated from

$$\bar{Q}_m = c_p \bar{\rho} \bar{u} S (\bar{T}_2 - \bar{T}_1). \quad (31)$$

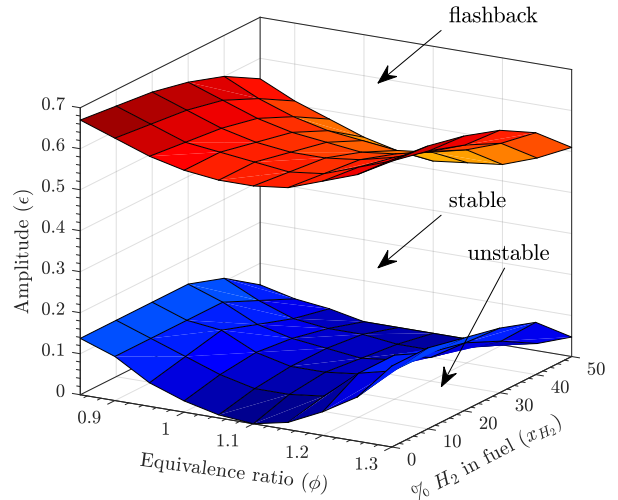


Figure 14: Three-dimensional stability-flashback map in $\phi - \chi_{H_2} - \varepsilon$ space.

For the χ_{H_2} range and ϕ range considered here, \bar{T}_2 varies in the range [2225, 2259] K. As a result, the speed of sound c_2 varies in the range [892, 910] ms^{-1} , and the frequency ω_1 of the first Green's function mode varies between [172, 450] $2\pi\text{s}^{-1}$.

For the thermoacoustic stability predictions, we solved Eq. (30) to obtain the thermoacoustic eigenfrequencies Ω_m , and hence $\text{Im} \Omega_m$; only the first mode, $m = 1$, was considered. The function $h_\varepsilon(t)$ was a superposition of three Gauss curves with amplitude-dependent fitting parameters $n_1, n_2, n_3, \tau_1, \tau_2, \tau_3, \sigma_1, \sigma_2, \sigma_3$ as described in Section 3.2. For the flashback predictions, we used Eq. (12). The stability predictions are shown in Fig. 14.

The region above the red surface is where there is a risk of flashback. The blue surface separates the regions of unstable and stable thermoacoustic oscillations. If the initial amplitude of the oscillation is small enough to be below the blue surface, the amplitude will grow until it reaches the blue surface. At that point, the amplitude remains constant,

Table 3
Parameters describing the system under consideration

Parameter	Symbol	Numerical value	Units
length of tube	L	0.5	m
axial position of perforated plate	x_q	0.2	m
radius of perforations	R	0.001	m
perforation density	\mathcal{N}	1.09×10^5	holes per m ²
mean flow velocity	\bar{u}	1.0	m s ⁻¹
temperature in cold region	\bar{T}_1	300	K
speed of sound in cold region	c_1	345	m s ⁻¹
mean density in cold region	$\bar{\rho}$	1.2	kg m ⁻³
specific heat ratio	γ	1.4	
heat capacity at constant pressure	c_p	1010	m ² s ⁻² K ⁻¹

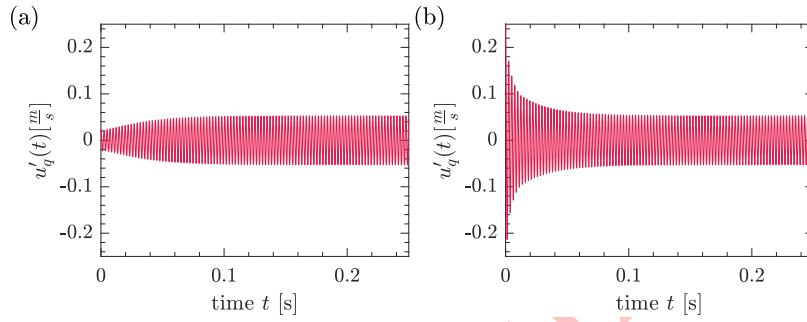


Figure 15: Time history of $u'_q(t)$ for $\chi_{H_2} = 20\%$ and $\phi = 1.0$. (a) Unstable case with small initial amplitude ($\varepsilon = 0.025$); (b) stable case with large initial amplitude ($\varepsilon = 0.25$).

i.e. a stable limit cycle has formed. If the thermoacoustic oscillation has an initial amplitude *above* the blue surface, its amplitude will decay until it reaches the blue surface, from where it will enter a stable limit cycle.

These two scenarios are illustrated in Fig. 15 for $\chi_{H_2} = 20\%$, $\phi = 1.0$ and two initial ε values: one below and one above the blue surface. Figure 15(a) shows the time history $u'_q(t)$ starting with $\varepsilon = 0.025$, and Fig. 15(b) shows $u'_q(t)$ starting with $\varepsilon = 0.25$ (both were calculated from Eq. (27) by a time-stepping approach; for details see [33]).

The time history in Fig. 15(a) starts with a growing amplitude and soon reaches a limit cycle with amplitude $\varepsilon = 0.05$. In Fig. 15(b), the oscillation decays at first until it reaches a limit cycle with the same amplitude.

The region between the blue and red surface in Fig. 14 can be considered as the region where safe operation is possible. We explore this in more detail in the next section.

5.3. Influence of the hydrogen concentration and equivalence ratio

Figure 16 presents the influence of the hydrogen concentration χ_{H_2} . It shows contour plots in the $\chi_{H_2} - \varepsilon$ plane for $\text{Re } \Omega_m$ and $\text{Im } \Omega_m$ ($m = 1$). Results are given only for the region where flashback does not occur; this is demarcated by the dotted red curve.

We observe the following trends as the hydrogen fraction χ_{H_2} increases:

- The thermoacoustic eigenfrequencies, $\text{Re } \Omega_1$, increase.

- The risk of instability decreases.
- The risk of flashback increases.

The reason for the increase in the eigenfrequencies is due to the following causal chain: an increase in χ_{H_2} increases the adiabatic flame temperature; this increases the temperature in the hot section of the combustion chamber, which leads to a higher speed of sound. For example, for a stoichiometric mixture of hydrogen and natural gas: $T_{ad} = 2225$ K if $\chi_{H_2} = 0\%$, whereas $T_{ad} = 2380$ K if $\chi_{H_2} = 100\%$ [37, 38]. Changes in χ_{H_2} also affect any time-lags between the heat release rate $Q'_m(t)$ and the acoustic field. According to the Rayleigh criterion [39, Section 6.2], this leads to the variations in the stability behaviour shown in Fig. 16(b). The risk of flashback increases because an increase in χ_{H_2} leads to shorter flames, and these are more prone to flashback.

Figure 17 presents the influence of the equivalence ratio ϕ in detail, showing the results for $\text{Re } \Omega_m$ and $\text{Im } \Omega_m$ ($m = 1$) as a contour plot in the $\phi - \varepsilon$ plane.

In Fig. 17, there are three distinct sections along the ϕ -axis: $\phi < 1$ (lean mixture), $\phi = [1 \dots 1.15]$ (near-stoichiometric mixture), and $\phi > 1.15$ (rich mixture). We observe the following trends as the equivalence ratio ϕ varies:

- The eigenfrequencies are largest in the range $\phi = [1 \dots 1.15]$ and decrease for ϕ -values on either side of this range (see Fig. 17(a)).

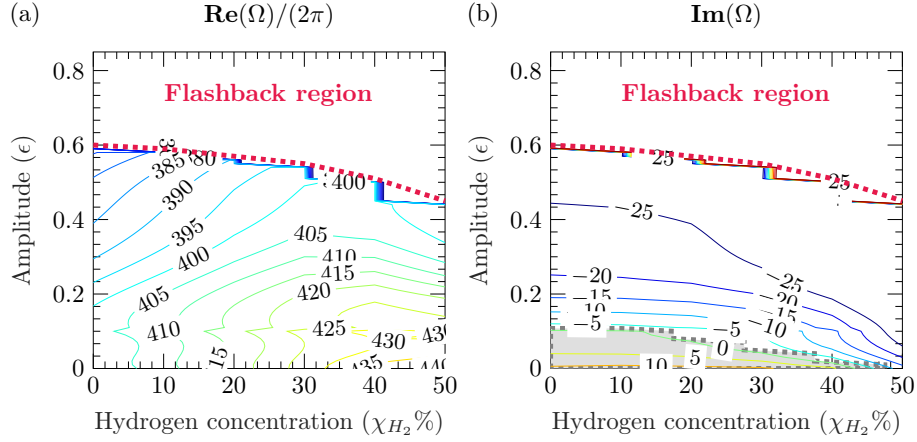


Figure 16: Results in the $\chi_{H_2} - \epsilon$ plane for $\phi = 1$. The dotted red line demarcates the flashback region. (a) Contours of the frequency $\text{Re}\Omega_1/2\pi$ (in Hz); (b) contours of the growth rate $\text{Im}\Omega_1$; the dotted grey curve marks the boundary between the stable and unstable region, and the grey shading indicates the unstable region.

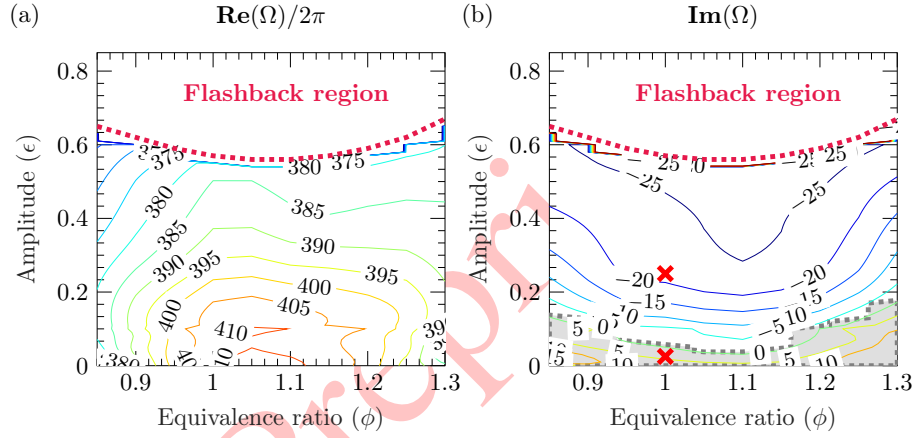


Figure 17: Results in the $\phi - \epsilon$ plane for $\chi_{H_2} = 20\%$. The dotted red line demarcates the flashback region. (a) Contours of the frequency $\text{Re}\Omega_1/2\pi$ (in Hz); (b) contours of the growth rate $\text{Im}\Omega_1$; the dotted grey curve marks the boundary between the stable and unstable region, and the grey shading indicates the unstable region. The two red crosses \times mark the initial amplitudes that were assumed to produce the time histories shown in Fig. 15.

- The risk of instability has a minimum in the range $\phi = [1 \dots 1.15]$, and increases for ϕ -values on either side of this range (see Fig. 17(b)).
- The risk of flashback shows the opposite trend: it occurs at amplitudes as low as $\epsilon=0.6$ for ϕ -values in the range $\phi = [1 \dots 1.15]$; for ϕ -values outside of this range, flashback occurs only at higher amplitudes.

These behaviours can be explained in terms of the S_L dependence on ϕ shown in Fig. 13(b). The relevant curve is that for $\chi_{H_2} = 20\%$. The S_L -value is maximum in the range $\phi = [1 \dots 1.15]$, but lower for $\phi < 1$ and $\phi > 1.15$. As a consequence, the flame is shorter for near-stoichiometric mixtures than for lean or rich mixtures.

It is evident from Figs. 16 and 17 that low values of χ_{H_2} favour instability, while high values of χ_{H_2} favour flashback. In terms of equivalence ratio, stability as well as flashback are favoured near stoichiometric combustion, i.e. for $\phi \approx 1$.

6. Conclusions and outlook

This paper presents a fundamental study on the dynamics of a laminar hydrogen-blend flame; the results of this study are then applied to predict the safe operating limits of a generic combustion test rig with a hydrogen-blend flame anchored on a perforated plate. The combustion chamber is an acoustic resonator, and this is modelled by the tailored Green's function, i.e. by the impulse response of the resonator. The flame is modelled by the classical G-equation, which describes the flame response to convected velocity fluctuations; the key parameter is the laminar flame speed S_L .

Insights from the fundamental study (flame dynamics)

The flame front stabilises at a location where the flame-normal velocity component is equal to S_L . As such, for a given incoming mean flow velocity, an increase in S_L

will lead to shorter and flatter flames, resulting in reduced travel distances and reduced travel times for convection and restoration waves along the flame front. It had been expected that for very low amplitudes of excitation (with a velocity amplitude as low as 2% of the mean flow velocity), the flame dynamics would be linear, i.e. the flame tip would oscillate around the position of the steady flame tip. However, we have observed that even at very low amplitudes, the flame shows nonlinear behaviour: the flame tip oscillates around a mean position that is *below* the position of the steady flame tip. This effect becomes more pronounced for higher amplitudes: the more the amplitude increases, the more the mean position of the oscillating flame tip shifts downwards. Hence the actual convection and restoration times are always lower than the values that would be predicted from a linear flame model. Additionally, a substantial reduction in the effective mean flame height is brought about by flame pinching. This leads to a significant reduction in the convection time (without any changes in S_L), and the disappearance of restoration waves.

Insights from the applied study (complete combustion test rig)

Since the flame dynamics depends on S_L , which in turn depends on the hydrogen concentration χ_{H_2} and the equivalence ratio ϕ , our stability analysis involved the following three parameters: χ_{H_2} , ϕ and the amplitude ε . A large range of stable operation was identified in the parameter space for ε -values, especially in the mid-range. Low ε -values bring an increased risk of thermoacoustic instability, while high ε -values bring a risk of flashback. Unstable oscillations develop into limit cycles, and their amplitudes depend on χ_{H_2} and ϕ .

Acknowledgements

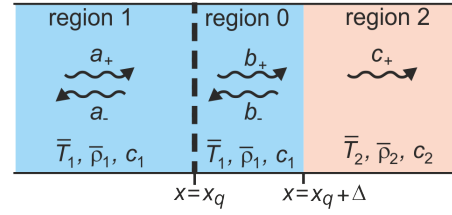
We are grateful to Thomas Steinbacher from the Technical University of Munich (now at IfTA GmbH), for making his GFlame code available to us so that we could calculate the flame describing functions shown in Section 3.1. This work was part of the HyDeploy project, which received financial support from Ofgem via the National Grid UK (grant reference NGGDGN03/1).

Appendix A. Model for the reflection and transmission of acoustic waves at the interface

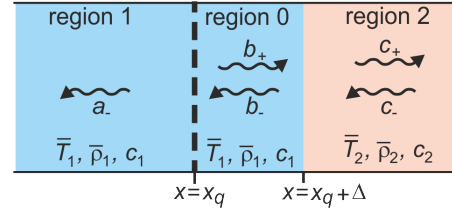
$x = x_q$

We consider an infinitely long tube with three regions as shown in Fig. A1. The interface between region 1 and region 0 is a perforated plate, and the interface between region 0 and region 2 is a temperature jump. The two interfaces are spaced a small distance Δ apart.

At the interface, which separates region 1 and region 0, we call the reflection and transmission coefficients R_{10} , T_{10} for forward transmission, and R_{01} , T_{01} for backward transmission. Similarly, at the interface between region 0 and



(a) incident wave coming from the upstream side



(b) incident wave coming from the downstream side

Figure A1: Waves reflected at the interfaces $x = x_q$ (perforated plate) and $x = x_q + \Delta$ (temperature jump).

region 2, we use R_{02} , T_{02} for forward transmission and R_{20} , T_{20} for backward transmission. The reflection and transmission coefficients of these interfaces, i.e. the perforated plate and the temperature jump, are known.

For the perforated plate, they are given by [39, p. 361]

$$R_{10} = R_{01} = \frac{\omega}{\omega + 2i\mathcal{N}c_1\mathcal{K}}, \quad T_{10} = T_{01} = \frac{2i\mathcal{N}c_1\mathcal{K}}{\omega + 2i\mathcal{N}c_1\mathcal{K}}, \quad (\text{A.1a,b})$$

where \mathcal{N} is the number of holes per unit area, c_1 is the speed of sound, and \mathcal{K} is the Rayleigh conductivity. For a plate of thickness h_p , with circular holes of radius r_p , \mathcal{K} is given by (see [39, p. 356])

$$\mathcal{K} = \frac{r_p^2\pi}{r_p\pi/2 + h_p}. \quad (\text{A.2})$$

The temperature jump has reflection and transmission coefficients given by [40, Section 4.1]

$$R_{02} = \frac{\bar{\rho}_2c_2 - \bar{\rho}_1c_1}{\bar{\rho}_2c_2 + \bar{\rho}_1c_1}, \quad T_{02} = \frac{2\bar{\rho}_2c_2}{\bar{\rho}_2c_2 + \bar{\rho}_1c_1} \quad (\text{A.3a,b})$$

for an incident wave coming from the upstream side. For an incident wave coming from the downstream side, the coefficients R_{20} and T_{20} are given by the same kind of expressions, but with $\bar{\rho}_1c_1$ and $\bar{\rho}_2c_2$ swapped over.

The individual interfaces can be lumped together into a single interface by the wave-based approach described for a more basic configuration in [34]. We first consider the case, shown in Fig. A1(a), where the incident wave comes from the upstream side. The pressure field in the three regions of the tube is

$$\hat{p}(x, \omega) = \begin{cases} a_+ e^{ik_1(x-x_q)} + a_- e^{-ik_1(x-x_q)} & \text{for region 1} \\ b_+ e^{ik_1(x-x_q)} + b_- e^{-ik_1(x-x_q)} & \text{for region 0} \\ c_+ e^{ik_2(x-x_q)} & \text{for region 2} \end{cases}$$

(A.4)

a_+ , a_- , b_+ , b_- , c_+ are the pressure amplitudes of the individual waves, and $k_1 = \omega/c_1$, $k_2 = \omega/c_2$ are their wave numbers. The reflection and transmission coefficients of the combined interface are

$$R_{12} = \lim_{\Delta \rightarrow 0} \frac{a_-}{a_+} \quad \text{and} \quad T_{12} = \lim_{\Delta \rightarrow 0} \frac{c_+}{a_+}. \quad (\text{A.5a,b})$$

In order to calculate them, we express the waves travelling away from the individual interfaces in terms of reflected and transmitted components.

$$\text{At } x = x_q: \quad a_- = R_{10} a_+ + T_{01} b_- \quad (\text{A.6a})$$

$$b_+ = R_{01} b_- + T_{10} a_+ \quad (\text{A.6b})$$

$$\text{At } x = x_q + \Delta: \quad b_- e^{-ik_1 \Delta} = R_{02} b_+ e^{ik_1 \Delta} \quad (\text{A.6c})$$

$$c_+ e^{ik_2 \Delta} = T_{02} b_+ e^{ik_1 \Delta} \quad (\text{A.6d})$$

Eqs. (A.6a-d) can be written as a matrix equation for the unknowns a_- , b_+ , b_- , c_+ as,

$$\begin{bmatrix} -1 & 0 & T_{01} & 0 \\ 0 & -1 & R_{01} & 0 \\ 0 & R_{02} e^{ik_1 \Delta} & -e^{-ik_1 \Delta} & 0 \\ 0 & T_{02} e^{ik_1 \Delta} & 0 & -e^{-ik_2 \Delta} \end{bmatrix} \begin{bmatrix} a_- \\ b_+ \\ b_- \\ c_+ \end{bmatrix} = a_+ \begin{bmatrix} -R_{10} \\ -T_{10} \\ 0 \\ 0 \end{bmatrix} \quad (\text{A.7})$$

and solved by Cramer's rule. For the unknowns a_- and c_+ , one obtains

$$a_- = a_+ \frac{R_{10} e^{-ik_1 \Delta} - R_{10} R_{01} R_{02} e^{ik_1 \Delta} + T_{10} T_{01} R_{02} e^{ik_1 \Delta}}{e^{-ik_1 \Delta} - R_{01} R_{02} e^{ik_1 \Delta}} \quad (\text{A.8a})$$

$$c_+ = a_+ \frac{T_{10} T_{02}}{e^{ik_2 \Delta} [e^{-ik_1 \Delta} - R_{01} R_{02} e^{ik_1 \Delta}]} \quad (\text{A.8b})$$

This leads immediately to the amplitude ratios in Eqs. (A.5a,b). After letting $\Delta \rightarrow 0$, one obtains

$$R_{12} = \lim_{\Delta \rightarrow 0} \frac{a_-}{a_+} = \frac{R_{10} - R_{10} R_{01} R_{02} + T_{10} T_{01} R_{02}}{1 - R_{01} R_{02}}, \quad (\text{A.9a})$$

$$T_{12} = \lim_{\Delta \rightarrow 0} \frac{c_+}{a_+} = \frac{T_{10} T_{02}}{1 - R_{01} R_{02}}. \quad (\text{A.9b})$$

For transmission in the opposite direction, i.e. from region 2 to region 1 (see Fig. A1(b)), we get expressions analogous to Eqs. (A.9a,b), with the subscripts 1 and 2 swapped over,

$$R_{21} = \frac{R_{20} - R_{20} R_{02} R_{01} + T_{20} T_{02} R_{01}}{1 - R_{01} R_{02}}, \quad (\text{A.10a})$$

$$T_{21} = \frac{T_{20} T_{01}}{1 - R_{01} R_{02}}. \quad (\text{A.10b})$$

Appendix B. Derivation of Eq. (30) for the complex eigenfrequencies Ω_m

The starting point of our derivation is the integral equation Eq. (27)

$$u'_q(t) = -\frac{\gamma-1}{c^2} \int_{t^*=0}^t H(t-t^*) \text{Re} \left[\sum_{n=1}^{\infty} G_n e^{-i\omega_n(t-t^*)} \right] q(t^*) dt^* - \frac{1}{c^2} \text{Re} \left[\sum_{n=1}^{\infty} G_n e^{-i\omega_n t} (i\omega_n \varphi_0 - \dot{\varphi}_0) \right]. \quad (\text{B.1})$$

We use $\text{Re } z = \frac{1}{2}(z + \bar{z})$, which holds for any complex quantity z and its complex conjugate \bar{z} , to rewrite the real parts in the equation above. This gives

$$u'_q(t) = -\frac{\gamma-1}{2c^2} \int_{t^*=0}^t \sum_{n=1}^{\infty} \left[G_n e^{-i\omega_n(t-t^*)} + \tilde{G}_n e^{i\tilde{\omega}_n(t-t^*)} \right] q(t^*) dt^* - \frac{1}{2c^2} \sum_{n=1}^{\infty} \left[G_n e^{-i\omega_n t} (i\omega_n \varphi_0 - \dot{\varphi}_0) + \tilde{G}_n e^{i\tilde{\omega}_n t} (-i\tilde{\omega}_n \varphi_0 - \dot{\varphi}_0) \right]. \quad (\text{B.2})$$

For $q(t)$, we use Eq. (15),

$$q(t) = \frac{Q'_m(t)}{\bar{\rho} S} = K \int_{\tau=0}^{\infty} h_\varepsilon(\tau) u'_q(t-\tau) d\tau, \quad (\text{B.3})$$

with

$$K = \frac{\bar{Q}_m}{S \bar{\rho} u} = c_p \Delta T, \quad (\text{B.4})$$

where c_p is the heat capacity at constant pressure, and ΔT is the temperature difference between the hot and the cold region. $h_\varepsilon(t)$ denotes the superposition of Gauss distributions given in Eq. (11), with ε -dependent fitting parameters. For $u'_q(t-\tau)$, we use

$$u'_q(t-\tau) = \sum_{m=1}^{\infty} \left(u_m e^{-i\Omega_m(t-\tau)} + \tilde{u}_m e^{i\tilde{\Omega}_m(t-\tau)} \right) \quad (\text{B.5})$$

(see Eq. (29)), and then $q(t^*)$ becomes

$$q(t^*) = K \int_{\tau=0}^{\infty} h_\varepsilon(\tau) \sum_{m=1}^{\infty} \left(u_m e^{-i\Omega_m(t^*-\tau)} + \tilde{u}_m e^{i\tilde{\Omega}_m(t^*-\tau)} \right) d\tau. \quad (\text{B.6})$$

Substitution of Eq. (B.6) into Eq. (B.2) gives

$$u'_q(t) =$$

$$\boxed{
 \begin{aligned}
 & -\frac{\gamma-1}{2c^2} \int_{t^*=0}^t \left\{ \sum_{n=1}^{\infty} \left[G_n e^{-i\omega_n(t-t^*)} + \tilde{G}_n e^{i\tilde{\omega}_n(t-t^*)} \right] \times \right. \\
 & \left. K \int_{\tau=0}^{\infty} h_{\varepsilon}(\tau) \sum_{m=1}^{\infty} \left[u_m e^{-i\Omega_m(t^*-\tau)} + \tilde{u}_m e^{i\tilde{\Omega}_m(t^*-\tau)} \right] d\tau \right\} dt^*
 \end{aligned}
 }$$

$$\begin{aligned}
 & -\frac{1}{2c^2} \sum_{n=1}^{\infty} \left[G_n e^{-i\omega_n t} (i\omega_n \varphi_0 - \dot{\varphi}_0) \right. \\
 & \left. + \tilde{G}_n e^{i\tilde{\omega}_n t} (-i\tilde{\omega}_n \varphi_0 - \dot{\varphi}_0) \right] \quad (\text{B.7})
 \end{aligned}$$

We call the first term on the right hand side of the above equation RHS_1 (the term inside the box) and manipulate it in several steps. First, we multiply out the square brackets to get

$$\begin{aligned}
 \text{RHS}_1 = & \\
 & -\frac{\gamma-1}{2c^2} K \int_{\tau=0}^{\infty} h_{\varepsilon}(\tau) \sum_{m,n=1}^{\infty} \int_{t^*=0}^t \left[G_n u_m e^{-i\omega_n(t-t^*)} e^{-i\Omega_m(t^*-\tau)} \right. \\
 & + G_n \tilde{u}_m e^{-i\omega_n(t-t^*)} e^{i\tilde{\Omega}_m(t^*-\tau)} \\
 & + \tilde{G}_n u_m e^{i\tilde{\omega}_n(t-t^*)} e^{-i\Omega_m(t^*-\tau)} \\
 & \left. + \tilde{G}_n \tilde{u}_m e^{i\tilde{\omega}_n(t-t^*)} e^{i\tilde{\Omega}_m(t^*-\tau)} \right] dt^* d\tau. \quad (\text{B.8})
 \end{aligned}$$

Next, we combine the t^* -dependent terms and integrate with respect to t^* ; this gives

$$\begin{aligned}
 \text{RHS}_1 = & \\
 & -\frac{\gamma-1}{2c^2} K \int_{\tau=0}^{\infty} h_{\varepsilon}(\tau) \sum_{m,n=1}^{\infty} \left[G_n u_m e^{-i\omega_n t} e^{i\Omega_m \tau} \frac{e^{i(\omega_n - \Omega_m)t} - 1}{i(\omega_n - \Omega_m)} \right. \\
 & + G_n \tilde{u}_m e^{-i\omega_n t} e^{-i\tilde{\Omega}_m \tau} \frac{e^{i(\omega_n + \tilde{\Omega}_m)t} - 1}{i(\omega_n + \tilde{\Omega}_m)} \\
 & + \tilde{G}_n u_m e^{i\tilde{\omega}_n t} e^{i\Omega_m \tau} \frac{e^{i(-\tilde{\omega}_n - \Omega_m)t} - 1}{i(-\tilde{\omega}_n - \Omega_m)} \\
 & \left. + \tilde{G}_n \tilde{u}_m e^{i\tilde{\omega}_n t} e^{-i\tilde{\Omega}_m \tau} \frac{e^{i(-\tilde{\omega}_n + \tilde{\Omega}_m)t} - 1}{i(-\tilde{\omega}_n + \tilde{\Omega}_m)} \right] d\tau \quad (\text{B.9})
 \end{aligned}$$

We then combine the exponential terms that have a t -dependence to get

$$\begin{aligned}
 \text{RHS}_1 = & \\
 & -\frac{\gamma-1}{2c^2} K \int_{\tau=0}^{\infty} h_{\varepsilon}(\tau) \sum_{m,n=1}^{\infty} \left[G_n u_m e^{i\Omega_m \tau} \frac{e^{-i\Omega_m t} - e^{-i\omega_n t}}{i(\omega_n - \Omega_m)} \right. \\
 & + G_n \tilde{u}_m e^{-i\tilde{\Omega}_m \tau} \frac{e^{i\tilde{\Omega}_m t} - e^{-i\omega_n t}}{i(\omega_n + \tilde{\Omega}_m)} \\
 & \left. + \tilde{G}_n u_m e^{i\Omega_m \tau} \frac{e^{-i\Omega_m t} - e^{i\tilde{\omega}_n t}}{i(-\tilde{\omega}_n - \Omega_m)} \right.
 \end{aligned}$$

$$\left. + \tilde{G}_n \tilde{u}_m e^{-i\tilde{\Omega}_m \tau} \frac{e^{i\tilde{\Omega}_m t} - e^{i\tilde{\omega}_n t}}{i(-\tilde{\omega}_n + \tilde{\Omega}_m)} \right] d\tau. \quad (\text{B.10})$$

This expression contains the following four t -dependent terms: $e^{-i\Omega_m t}$, $e^{i\tilde{\Omega}_m t}$, $e^{-i\omega_n t}$ and $e^{i\tilde{\omega}_n t}$. We collect these terms and factorize with respect to them; this gives

$$\begin{aligned}
 \text{RHS}_1 = & -\frac{\gamma-1}{2c^2} K \int_{\tau=0}^{\infty} h_{\varepsilon}(\tau) \times \\
 & \left\{ \sum_{m=1}^{\infty} u_m e^{-i\Omega_m t} e^{i\Omega_m \tau} \sum_{n=1}^{\infty} \left[\frac{G_n}{i(\omega_n - \Omega_m)} + \frac{\tilde{G}_n}{i(-\tilde{\omega}_n - \Omega_m)} \right] \right. \\
 & + \sum_{m=1}^{\infty} \tilde{u}_m e^{i\tilde{\Omega}_m t} e^{-i\tilde{\Omega}_m \tau} \sum_{n=1}^{\infty} \left[\frac{G_n}{i(\omega_n + \tilde{\Omega}_m)} + \frac{\tilde{G}_n}{i(-\tilde{\omega}_n + \tilde{\Omega}_m)} \right] \\
 & + \sum_{n=1}^{\infty} G_n e^{-i\omega_n t} \sum_{m=1}^{\infty} \left[-\frac{u_m e^{i\Omega_m \tau}}{i(\omega_n - \Omega_m)} - \frac{\tilde{u}_m e^{-i\tilde{\Omega}_m \tau}}{i(\omega_n + \tilde{\Omega}_m)} \right] \\
 & \left. + \sum_{n=1}^{\infty} \tilde{G}_n e^{i\tilde{\omega}_n t} \sum_{m=1}^{\infty} \left[-\frac{u_m e^{i\Omega_m \tau}}{i(-\tilde{\omega}_n - \Omega_m)} - \frac{\tilde{u}_m e^{-i\tilde{\Omega}_m \tau}}{i(-\tilde{\omega}_n + \tilde{\Omega}_m)} \right] \right\} d\tau \quad (\text{B.11})
 \end{aligned}$$

We now return to Eq. (B.7), use the above result for RHS_1 , and substitute for $u'_q(t)$ with Eq. (29). This gives

$$\begin{aligned}
 & \sum_{m=1}^{\infty} \left(u_m e^{-i\Omega_m t} + \tilde{u}_m e^{i\tilde{\Omega}_m t} \right) = -\frac{\gamma-1}{2c^2} K \int_{\tau=0}^{\infty} h_{\varepsilon}(\tau) \times \\
 & \left\{ \sum_{m=1}^{\infty} u_m e^{-i\Omega_m t} e^{i\Omega_m \tau} \sum_{n=1}^{\infty} \left[\frac{G_n}{i(\omega_n - \Omega_m)} + \frac{\tilde{G}_n}{i(-\tilde{\omega}_n - \Omega_m)} \right] \right. \\
 & + \sum_{m=1}^{\infty} \tilde{u}_m e^{i\tilde{\Omega}_m t} e^{-i\tilde{\Omega}_m \tau} \sum_{n=1}^{\infty} \left[\frac{G_n}{i(\omega_n + \tilde{\Omega}_m)} + \frac{\tilde{G}_n}{i(-\tilde{\omega}_n + \tilde{\Omega}_m)} \right] \\
 & + \sum_{n=1}^{\infty} G_n e^{-i\omega_n t} \sum_{m=1}^{\infty} \left[-\frac{u_m e^{i\Omega_m \tau}}{i(\omega_n - \Omega_m)} - \frac{\tilde{u}_m e^{-i\tilde{\Omega}_m \tau}}{i(\omega_n + \tilde{\Omega}_m)} \right] \\
 & \left. + \sum_{n=1}^{\infty} \tilde{G}_n e^{i\tilde{\omega}_n t} \sum_{m=1}^{\infty} \left[-\frac{u_m e^{i\Omega_m \tau}}{i(-\tilde{\omega}_n - \Omega_m)} - \frac{\tilde{u}_m e^{-i\tilde{\Omega}_m \tau}}{i(-\tilde{\omega}_n + \tilde{\Omega}_m)} \right] \right\} d\tau \\
 & - \frac{1}{2c^2} \sum_{n=1}^{\infty} \left[G_n e^{-i\omega_n t} (i\omega_n \varphi_0 - \dot{\varphi}_0) \right. \\
 & \left. + \tilde{G}_n e^{i\tilde{\omega}_n t} (-i\tilde{\omega}_n \varphi_0 - \dot{\varphi}_0) \right] \quad (\text{B.12})
 \end{aligned}$$

The four t -dependent terms $e^{-i\Omega_m t}$, $e^{i\tilde{\Omega}_m t}$, $e^{-i\omega_n t}$ and $e^{i\tilde{\omega}_n t}$ are marked in the above equation by a blue rectangle. We equate their coefficients on either side of Eq. (B.12), and this gives 4 sets of equations. The coefficients of $e^{-i\Omega_m t}$ give

$$\begin{aligned}
 & \int_{\tau=0}^{\infty} h_{\varepsilon}(\tau) e^{i\Omega_m \tau} d\tau \sum_{n=1}^{\infty} \left[\frac{G_n}{i(\omega_n - \Omega_m)} - \frac{\tilde{G}_n}{i(\tilde{\omega}_n + \Omega_m)} \right] = \\
 & -\frac{2c^2}{K(\gamma-1)}, \quad m = 1, 2, \dots \quad (\text{B.13})
 \end{aligned}$$

which is Eq. (30) in the main text. The second set of equations comes from the coefficients of $e^{i\Omega_m t}$; this turns out to be the complex conjugate of Eq. (B.13). The coefficients of $e^{-i\omega_n t}$ and $e^{i\omega_n t}$ give the third and fourth set of equations; these turn out to be linear equations for the velocity amplitudes u_m and \tilde{u}_m .

CRedit authorship contribution statement

Sreenath Malamal Gopinathan: Conceptualization of this study, Formal Analysis, Investigation, Methodology, Software, Visualisation, Writing - original draft, Writing - review & editing. **Aswathy Surendran:** Conceptualization of this study, Formal Analysis, Investigation, Methodology, Writing - original draft, Writing - review & editing. **Maria A. Heckl:** Conceptualization of this study, Formal Analysis, Funding acquisition, Investigation, Methodology, Resources, Supervision, Writing - original draft, Writing - review & editing.

References

- [1] Rachele Lamioni, Cristiana Bronzoni, Marco Folli, Leonardo Tognotti, and Chiara Galletti. Impact of H₂-enriched natural gas on pollutant emissions from domestic condensing boilers: numerical simulations of the combustion chamber. *International Journal of Hydrogen Energy*, 48(51):19686–19699, June 2023. doi: 10.1016/j.ijhydene.2023.02.040.
- [2] Gianluca Rossiello, Muhammad Ali Uzair, Seyed Behzad Ahmadpanah, Lorenzo Morandi, Marzio Ferrara, Gabriele Domenico Rago, Giuseppe Molfetta, Alessandro Saponaro, and Marco Torresi. Design and testing of a multi-fuel industrial burner suitable for syn-gases, flare gas and pure hydrogen. *Thermal Science and Engineering Progress*, 42:101845, 2023. doi: 10.1016/j.tsep.2023.101845.
- [3] Muhammad Akasha Hashim, Amir Khalid, Hamidon Salleh, and Norsuhaila Mohamed Sunar. Effects of fuel and nozzle characteristics on micro gas turbine system: A review. *IOP Conference Series: Materials Science and Engineering*, 226(1):012006, August 2017. doi: 10.1088/1757-899X/226/1/012006.
- [4] Donato Cecere, Eugenio Giacomazzi, Antonio Di Nardo, and Giorgio Calchetti. Gas turbine combustion technologies for hydrogen blends. *Energies*, 16(19):6829, September 2023. doi: 10.3390/en16196829.
- [5] Binash A. Imteyaz, Medhat A. Nemitallah, Ahmed A. Abdelhafez, and Mohamed A. Habib. Combustion behavior and stability map of hydrogen-enriched oxy-methane premixed flames in a model gas turbine combustor. *International Journal of Hydrogen Energy*, 43(34):16652–16666, August 2018. doi: 10.1016/j.ijhydene.2018.07.087.
- [6] Haifeng Li and Jingran Chen. An analysis of long-process ironmaking in a reduction smelting furnace with hydrogen-enriched conditions. *Metals*, 13(10):1756, October 2023. doi: 10.3390/met13101756.
- [7] Paul Glanville, Alex Fridlyand, Brian Sutherland, Miroslaw Liszka, Yan Zhao, Luke Bingham, and Kris Jorgensen. Impact of hydrogen/natural gas blends on partially premixed combustion equipment: NO_x emission and operational performance. *Energies*, 15(5):1706, February 2022. doi: 10.3390/en15051706.
- [8] Devinder Mahajan, Kun Tan, T. Venkatesh, Pradheep Kileti, and Clive R. Clayton. Hydrogen blending in gas pipeline networks—a review. *Energies*, 15(10), 2022. doi: 10.3390/en15103582.
- [9] M. Fleifil, A.M. Annaswamy, Z.A. Ghoneim, and A.F. Ghoniem. Response of a laminar premixed flame to flow oscillations: A kinematic model and thermoacoustic instability results. *Combustion and Flame*, 106(4):487–510, September 1996. doi: 10.1016/0010-2180(96)00049-1.
- [10] Thierry Schuller, Sébastien Ducruix, Daniel Durox, and Sébastien Candel. Modeling tools for the prediction of premixed flame transfer functions. *Proceedings of the Combustion Institute*, 29(1):107–113, 2002. doi: 10.1016/S1540-7489(02)80018-9.
- [11] Karthik Kashinath, Santosh Hemchandra, and Matthew P. Juniper. Nonlinear thermoacoustics of ducted premixed flames: The influence of perturbation convection speed. *Combustion and Flame*, 160(12):2856–2865, 2013. doi: 10.1016/j.combustflame.2013.06.019.
- [12] Ralf S. Blumenthal, Priya Subramanian, R.I. Sujith, and Wolfgang Polifke. Novel perspectives on the dynamics of premixed flames. *Combustion and Flame*, 160(7):1215–1224, July 2013. doi: 10.1016/j.combustflame.2013.02.005.
- [13] A. Albayrak, R.S. Blumenthal, A. Ulhaq, and W. Polifke. An analytical model for the impulse response of laminar premixed flames to equivalence ratio perturbations. *Proceedings of the Combustion Institute*, 36(3):3725–3732, 2017. doi: 10.1016/j.proci.2016.06.002.
- [14] Thomas Steinbacher, Alp Albayrak, Abdulla Ghani, and Wolfgang Polifke. Consequences of flame geometry for the acoustic response of premixed flames. *Combustion and Flame*, 199:411–428, 2019. doi: 10.1016/j.combustflame.2018.10.039.
- [15] Eirik Æsøy, José G. Aguilar, Samuel Wiseman, Mirko R. Bothien, Nicholas A. Worth, and James R. Dawson. Scaling and prediction of transfer functions in lean premixed H₂/CH₄-flames. *Combustion and Flame*, 215:269–282, 2020. doi: 10.1016/j.combustflame.2020.01.045.
- [16] J.G. Aguilar, E. Æsøy, and J.R. Dawson. Predicting the influence of hydrogen in combustion instabilities. In *Symposium on Thermoacoustics in Combustion: Industry meets Academia (SoTiC 2021)*, held online, 06 – 10 September 2021.
- [17] Zhengli Lim, Jingxuan Li, and Aimee S. Morgans. The effect of hydrogen enrichment on the forced response of CH₄/H₂/air laminar flames. *International Journal of Hydrogen Energy*, 46:23943–23953, July 2021. doi: 10.1016/j.ijhydene.2021.04.171.
- [18] Efstathios Karlis, Yushuai Liu, Yannis Hardalupas, and Alexander M.K.P. Taylor. H₂ enrichment of CH₄ blends in lean premixed gas turbine combustion: An experimental study on effects on flame shape and thermoacoustic oscillation dynamics. *Fuel*, 254:115524, 2019. doi: 10.1016/j.fuel.2019.05.107.
- [19] H.H.-W. Funke, J. Dickhoff, J. Keinz, A. Haj Ayed, A. Parente, and P. Hendrick. Experimental and numerical study of the micromix combustion principle applied for hydrogen and hydrogen-rich syngas as fuel with increased energy density for industrial gas turbine applications. *Energy Procedia*, 61:1736–1739, 2014. doi: 10.1016/j.egypro.2014.12.201.
- [20] Jadeed Beita, Midhat Talibi, Suresh Sadasivuni, and Ramanarayanan Balachandran. Thermoacoustic instability considerations for high hydrogen combustion in lean premixed gas turbine combustors: A review. *Hydrogen*, 2(1):33–57, 2021. doi: 10.3390/hydrogen2010003.
- [21] Alan R. Kerstein, William T. Ashurst, and Forman A. Williams. Field equation for interface propagation in an unsteady homogeneous flow field. *Physical Review A*, 37(7):2728–2731, April 1988. doi: 10.1103/physreva.37.2728.
- [22] Ian M. Mitchell. A toolbox of level set methods. Technical Report TR-2007-11, University of British Columbia, Department of Computer Science, June 2007.
- [23] T. Steinbacher. *Analysis and low-order modeling of interactions between acoustics, hydrodynamics and premixed flames*. PhD thesis, Technical University of Munich, 2019.
- [24] A. Cuquel. *Dynamics and nonlinear thermo-acoustic stability analysis of premixed conical flames*. PhD thesis, Ecole Centrale Paris, 2013.
- [25] N. Noiray, D. Durox, T. Schuller, and S. Candel. A unified framework for nonlinear combustion instability analysis based on the flame describing function. *Journal of Fluid Mechanics*, 615:139–167, 2008. doi: 10.1017/S0022112008003613.

- [26] Nader Karimi, Michael J. Brear, Seong-Ho Jin, and Jason P. Monty. Linear and non-linear forced response of a conical, ducted, laminar premixed flame. *Combustion and Flame*, 156(11):2201–2212, 2009. doi: 10.1016/j.combustflame.2009.06.027.
- [27] J. W. S. Rayleigh. The explanation of certain acoustical phenomena. *Nature*, 18(455):319–321, 1878. doi: 10.1038/018319a0.
- [28] F. E. C. Culick. Short Communication. A note on Rayleigh’s criterion. *Combustion Science and Technology*, 56(4–6):159–166, December 1987. doi: 10.1080/00102208708947087.
- [29] Sreenath M Gopinathan, Alessandra Bigongiari, and Maria Heckl. Analytical approximations for heat release rate laws in the time- and frequency-domains. *International Journal of Spray and Combustion Dynamics*, 12, January 2020. doi: 10.1177/1756827720930491.
- [30] Sreenath M Gopinathan, Dmytro Iurashev, Alessandra Bigongiari, and Maria Heckl. Nonlinear analytical flame models with amplitude-dependent time-lag distributions. *International Journal of Spray and Combustion Dynamics*, 10(4):264–276, August 2017. doi: 10.1177/1756827717728056.
- [31] R Preetham, H. Santosh, and Tim Lieuwen. Dynamics of laminar premixed flames forced by harmonic velocity disturbances. *Journal of Propulsion and Power*, 24(6):1390–1402, November 2008. doi: 10.2514/1.35432.
- [32] Maria A. Heckl and M.S. Howe. Stability analysis of the Rijke tube with a Green’s function approach. *Journal of Sound and Vibration*, 305(4–5):672–688, September 2007. doi: 10.1016/j.jsv.2007.04.027.
- [33] Maria A. Heckl, Sreenath Malamal Gopinathan, and Aswathy Surendran. A unified framework for acoustic instabilities based on the tailored Green’s function. *Journal of Sound and Vibration*, 541: 117279, December 2022. doi: 10.1016/j.jsv.2022.117279.
- [34] Maria A. Heckl. Analytical model of nonlinear thermo-acoustic effects in a matrix burner. *Journal of Sound and Vibration*, 332(17): 4021–4036, August 2013. doi: 10.1016/j.jsv.2012.11.010.
- [35] Alessandra Bigongiari and Maria A. Heckl. A Green’s function approach to the rapid prediction of thermoacoustic instabilities in combustors. *Journal of Fluid Mechanics*, 798:970–996, June 2016. doi: 10.1017/jfm.2016.332.
- [36] Z Huang, Y Zhang, K Zeng, B Liu, Q Wang, and D Jiang. Measurements of laminar burning velocities for natural gas–hydrogen–air mixtures. *Combustion and Flame*, 146(1–2):302–311, July 2006. doi: 10.1016/j.combustflame.2006.03.003.
- [37] Sanford Gordon and Bonnie J. McBride. Computer program for calculation of complex chemical equilibrium compositions and applications : I. Analysis. Technical Report RP 1311-1, NASA, 1994.
- [38] Bonnie J. McBride and Sanford Gordon. Computer program for calculation of complex chemical equilibrium compositions and applications : II. User Manual and Description. NASA Reference Publication RP 1311, NASA, 1996.
- [39] M.S. Howe. *Acoustics of fluid-structure interaction*. Cambridge University Press, Cambridge, 1998.
- [40] A.P. Dowling and J.E. Ffowcs Williams. *Sound and sources of sound*. Ellis Horwood, Chichester, 1983.